# The Arctic Surface Heating Efficiency of Tropospheric Energy Flux Events

Christopher J. Cardinale[a] and Brian E. J. Rose,[a]

[a] *Department of Atmospheric and Environmental Sciences, University at Albany, State University of New York, Albany, New York*

*Corresponding author*: Christopher J. Cardinale, ccardinale@albany.edu



**Early Online Release**: This preliminary version has been accepted for publication in *Journal of Climate*, may be fully cited, and has been assigned DOI 10.1175/JCLI-D-21-0852.1. The final typeset copyedited article will replace the EOR at the above DOI when it is published.

ABSTRACT: This paper examines the processes that drive Arctic anomalous surface warming and sea ice loss during winter-season tropospheric energy flux events, synoptic periods of increased tropospheric energy flux convergence ($F_{\text{trop}}$), using the NASA MERRA-2 reanalysis. During an event, a poleward anomaly in $F_{\text{trop}}$ initially increases the sensible and latent energy of the Arctic troposphere; as the warm and moist troposphere loses heat, the anomalous energy source is balanced by a flux upward across the tropopause and a downward net surface flux. A new metric for the Arctic surface heating efficiency ($E_{\text{trop}}$) is defined, which measures the fraction of the energy source that reaches the surface. Composites of high, medium, and low-efficiency events help identify key physical factors, including the vertical structure of $F_{\text{trop}}$ and Arctic surface preconditioning. In high-efficiency events ($E_{\text{trop}} \geq 0.63$), a bottom-heavy poleward $F_{\text{trop}}$ occurs in the presence of an anomalously warm and unstratified Arctic—a consequence of decreased sea ice—resulting in increased vertical mixing, enhanced near-surface warming and moistening, and further sea ice loss. Smaller $E_{\text{trop}}$, and thus weaker surface impacts, are found in events with anomalously large initial sea ice extent and more vertically uniform $F_{\text{trop}}$. These differences in $E_{\text{trop}}$ are manifest primarily through turbulent heat fluxes rather than downward longwave radiation. The frequency of high-efficiency events has increased from the period 1980–1999 to 2000–2019, contributing to Arctic surface warming and sea ice decline.



Accepted for publication in *Journal of Climate*. DOI 10.1175/JCLI-D-21-0852.1.

## 1. Introduction

Observations over the past several decades indicate a bottom-amplified warming of the Arctic, with surface air temperatures increasing at a faster rate than the global average, especially during the cold season (Screen and Simmonds 2010a; Cohen et al. 2014). Winter sea ice has also declined in recent decades, especially in the Barents–Kara Seas where relatively large reductions in sea ice concentration (SIC; D.-S. R. Park et al. 2015) and thickness (King et al. 2017) have been observed. Although there exists a strong negative correlation between winter sea ice growth and November sea ice thickness (i.e., thin ice grows thermodynamically faster than thick ice), the influence of atmospheric forcing on the thinning sea ice has been increasing (Stroeve et al. 2018). It has been suggested that increased surface downward longwave radiation (DLR) is an important driver—perhaps the main driver—of trends in surface temperature (e.g., Woods and Caballero 2016; Gong et al. 2017; Lee et al. 2017) and sea ice (e.g., D.-S. R. Park et al. 2015; H.-S. Park et al. 2015; Woods and Caballero 2016), while increased ocean-to-atmosphere fluxes (i.e., the ice-albedo or insulation feedback; Screen and Simmonds 2010b; Stroeve et al. 2012; Burt et al. 2016) play a minor role. The DLR trend has been attributed to an increased frequency of intense tropospheric heat and moisture fluxes (i.e., moist intrusion events; Woods and Caballero 2016) into the Arctic (D.-S. R. Park et al. 2015; H.-S. Park et al. 2015; Woods and Caballero 2016; Gong et al. 2017; Lee et al. 2017). A recent study showed that in a mean climatic state, DLR is largely determined by surface temperatures (Vargas Zeppetello et al. 2019). For example, an increase in surface temperature warms and moistens the boundary layer through upward turbulent energy fluxes, inducing increased DLR; thus, it is difficult to determine if increased DLR is the dominant driver or largely a diagnostic of surface temperatures. Therefore, the processes that drive the Arctic surface response during moist intrusion events are not fully understood.

The Arctic surface response—mainly in the Barents–Kara Sea region—associated with synoptic-scale winter-season poleward tropospheric energy flux events has been a focus of numerous studies (e.g., Doyle et al. 2011; Yoo et al. 2012; Woods et al. 2013; D.-S. R. Park et al. 2015; H.-S. Park et al. 2015; Baggett and Lee 2015; Woods and Caballero 2016; Luo et al. 2016; Baggett and Lee 2017; Gong et al. 2017; Gong and Luo 2017; Luo et al. 2017; Johansson et al. 2017; Zhong et al. 2018; Liu et al. 2018; Chen et al. 2018; Luo et al. 2019; Tyrlis et al. 2019; Graham et al. 2019b). In general, these events are associated with the following temporal structure:



Accepted for publication in *Journal of Climate*. DOI 10.1175/JCLI-D-21-0852.1.

1) Anomalous tropospheric sensible and latent heat flux convergence contribute to the warming and moistening of the troposphere over the region and at the pressure level of the anomalous convergence. These events preferentially occur over the Atlantic sector of the Arctic basin (approximately 20°W to 80°E) and are associated with atmospheric blocking over the Ural Mountains [i.e., Ural blocking (UB)].

2) The anomalously warm and moist troposphere with increased cloudiness increases the DLR at the surface (mainly over sea ice), initiating surface heating (i.e., reduced surface heat loss and the reduced growth or melting of sea ice). Moisture and clouds contribute to increased DLR through increased atmospheric emissivity (Graversen and Burtu 2016), which reduces the longwave cooling efficiency of the Arctic atmosphere and surface (Hegyi and Taylor 2018). Increased surface air temperatures and specific humidity also suppress upward surface turbulent sensible and latent heat fluxes (SHLH), reducing surface heat loss (mainly over open ocean). Storm driven mixing of warm Atlantic water likely causes further ice melt.

3) Reduced SIC and increased sea surface temperatures are followed by enhanced upward SHLH, contributing to the warming of the lower-troposphere at the expense of the surface.

The initial state and response of the Arctic surface can differ for individual tropospheric energy flux events. Tropical convection in the Pacific warm pool can trigger planetary scale waves that amplify the climatological stationary wave pattern, initially driving adiabatic warming in the Arctic and subsequently driving long duration surface warming associated with large eddy fluxes of sensible and latent heat and increased DLR (Yoo et al. 2012; Baggett and Lee 2015, 2017). Additionally, the initial state and response of the Arctic surface during an event appears sensitive to the type of atmospheric blocking pattern (Chen et al. 2018; Luo et al. 2019). Chen et al. (2018) found that more persistent UB events are associated with an initially lower SIC and a more intense surface response in the Barents–Kara Seas due to increased moisture and DLR as opposed to suppressed SHLH. However, Chen et al. (2018) only focused on surface fluxes over areas of majority sea ice, likely reducing contributions from SHLH. More importantly, the potential large contributions to increased DLR from the surface warming itself—suggested by the work of Vargas Zeppetello et al. (2019)—questions the dominant role of increased moisture in driving the surface response and variability in the surface response.





Accepted for publication in *Journal of Climate*. DOI 10.1175/JCLI-D-21-0852.1.

The increased frequency of events over recent decades—consistent with the increased duration (Rinke et al. 2017) or frequency (Valkonen et al. 2021) of Arctic cyclones—is potentially driven by the increased occurrence of La Niña–like tropical convection over the Pacific warm pool (Baggett and Lee 2017) or an increased frequency of UB events (Luo et al. 2016; Rinke et al. 2017; Gong and Luo 2017; Chen et al. 2018; Luo et al. 2019). Interestingly, the increased UB frequency could be driven by reduced sea ice in the Barents–Kara Seas and the associated atmospheric circulation response, a potential positive feedback mechanism (Gong and Luo 2017; Chen et al. 2018). However, Peings (2019) found no significant atmospheric response in model simulations with perturbed ice in the Barents–Kara Seas. The divergence between modeling and observational studies potentially results from models underestimating the role of sea ice in driving an atmospheric circulation response (Overland et al. 2021) or from a misinterpretation of causality—atmospheric circulation anomalies drive rather than respond to sea ice anomalies (Blackport et al. 2019).

The above review demonstrates that tropospheric energy flux events can drive Arctic surface warming and sea ice loss. Here we define these events as anomalous convergence of tropospheric fluxes of moist static energy (MSE; sensible, latent, and geopotential), denoted $F_{\mathrm{trop}}$ poleward of 70°N. Such anomalous $F_{\mathrm{trop}}$ events are associated with tropospheric warming and moistening and anomalously downward surface fluxes (increased DLR and suppressed SHLH). In addition, a fraction of the energy input by a poleward $F_{\mathrm{trop}}$ anomaly is lost upward across the tropopause and does not impact the Arctic surface (Cardinale et al. 2021). It is possible that the variability in the surface response to tropospheric energy flux events is explained by differences in the fraction of the total energy input that reaches the Arctic surface—a quantity we refer to as the surface heating *efficiency*. The processes that determine this heating efficiency are not well understood but are crucial for understanding how these events may change in a future warmer climate.

To this end, we define and compute a new metric for the Arctic surface heating efficiency. Specifically, this metric describes the fraction of the anomalous tropospheric energy source due to $F_{\mathrm{trop}}$ that is balanced by an anomalous net surface flux (NSF; combined turbulent heat and longwave fluxes) over the entire Arctic polar cap. Here, "anomalous" refers to deviations from the climatological seasonal cycle. The NSF is used as a proxy for surface changes as it can drive both surface temperature and sea ice variability.



Accepted for publication in *Journal of Climate*. DOI 10.1175/JCLI-D-21-0852.1.

We are particularly interested in the vertical structure of $F_{\text{trop}}$ and its coupling to the Arctic surface. In Cardinale et al. (2021), we analyzed the vertical structure of the MSE flux convergence and the Arctic surface response during $F_{\text{trop}}$ and stratospheric energy flux ($F_{\text{strat}}$) events (e.g., sudden stratospheric warmings) and found that a majority of the energy input by a poleward anomaly in $F_{\text{trop}}$—mainly in the lower troposphere—was balanced by the NSF, while a poleward anomaly in $F_{\text{strat}}$ had little influence on the NSF. This suggests that the surface heating efficiency is linked to the vertical structure of the MSE flux convergence. We hypothesize that concentrating the MSE flux convergence (i.e., atmospheric heating and moistening) closer to the surface increases the surface heating efficiency. It is possible that tropospheric energy flux events have a large variability in surface heating efficiency and that the role of atmospheric circulations on Arctic warming and sea ice loss during winter is best explained by changes in the efficiency of events as opposed to changes in the total frequency of events. Using the Modern-Era Retrospective Analysis for Research and Applications, version 2 (MERRA-2) reanalysis, we compute the Arctic surface heating efficiency of tropospheric energy flux events during winter from January 1980 to March 2020.

Several key findings of our study have not been suggested in previous literature. Here we give a brief summary of these results:

1) The vertical structure of the MSE flux convergence and the stability of the lower troposphere—associated with the initial state of the Arctic surface prior to the event—largely determine the surface heating efficiency of a tropospheric energy flux event.

2) Downward anomalies in surface turbulent heat fluxes (i.e., suppression of upward sensible and latent heat fluxes), as opposed to anomalous DLR, explain the majority of differences in the surface heating efficiency between events.

3) The surface heating efficiency of tropospheric energy flux events has increased, especially since 2004.

The efficiency metric will be introduced in section 2. An analysis of the efficiency of tropospheric energy flux events will be presented in section 3a, comparisons of events with different efficiencies will be presented in section 3b, and a trend analysis will be presented in section 3c.



Accepted for publication in *Journal of Climate*. DOI 10.1175/JCLI-D-21-0852.1.

## 2. Data and methods

### *a. MERRA-2 and the MSE flux*

We use winds, atmospheric temperatures (not including skin temperature), specific humidity, geopotential, radiative fluxes at the surface and top of atmosphere [TOA; i.e., outgoing longwave radiation (OLR)], surface turbulent energy fluxes, sea ice concentration (SIC), and cloud concentrations from MERRA-2. MERRA-2, the latest atmospheric reanalysis (1980–present) produced by NASA's Global Modeling and Assimilation Office (GMAO), has a horizontal resolution of 0.5° x 0.625°, 72 vertical levels with output interpolated to 42 pressure levels up to 0.1 hPa, and a temporal resolution of 3-hours (GMAO 2015). Winter seasons (NDJFM) from January 1980 to March 2020 are used in this analysis. An evaluation of the performance of surface fluxes in the MERRA-2 reanalysis over Arctic sea ice during winter can be found in Graham et al. (2019a). Compared to observations from the Norwegian Young sea ice campaign (N-ICE2015), MERRA-2 shows high skill in simulating downwelling longwave radiation and poor skill in simulating turbulent heat fluxes—similar to all reanalyses evaluated in Graham et al. (2019a). However, errors in the turbulent heat fluxes can be largely explained by differences in the point observations and the grid cell averages in MERRA-2, which contain a fraction of open ocean and larger mean upward turbulent fluxes relative to the point observations over sea ice (i.e., where the SIC is 100%). Despite large differences in mean cloud fractions between reanalyses and satellite products, MERRA-2 has demonstrated skill in estimating anomalous cloud fractions (Liu and Key 2016). More information on the evaluation of the climate in MERRA-2 can be found in Bosilovich et al. (2015), and information on input observations can be found in McCarty et al. (2016).

Fluxes of moist static energy (MSE) and contributions from the sensible heat (SH), latent heat (LH), and geopotential (GP) fluxes on pressure levels at 70°N are computed following Cardinale et al. (2021), where the flux was separated into contributions from the eddy and mean meridional circulation (MMC) flux, neglecting contributions from the net mass flux (NMF). Contributions to the total vertically integrated polar cap–averaged MSE flux convergence ($F_{\mathrm{wall}}$) from the troposphere ($F_{\mathrm{trop}}$) are obtained by integrating the flux from 1000 to 300 hPa. The MSE flux is computed instantaneously from the 3-hourly data and averaged daily. On pressure levels, the MSE flux and local contribution to the integrated MSE flux convergence have units of $\mathrm{J\,kg^{-1}\,m\,s^{-1}}$ and



Accepted for publication in *Journal of Climate.* DOI 10.1175/JCLI-D-21-0852.1.

$\mathrm{W\,m^{-2}\,(100\,hPa)^{-1}}$, respectively. Vertically integrated flux values (e.g, $F_{\mathrm{trop}}$) have units of $\mathrm{W\,m^{-2}}$ (expressed as a polar cap–averaged flux convergence) and time-integrated values have units of $\mathrm{MJ\,m^{-2}}$.

### b. A metric for the Arctic surface heating efficiency

We define the Arctic surface heating efficiency, $E_{\mathrm{trop}}$, as:

$$E_{\mathrm{trop}} = \frac{\langle \mathrm{NSF}' \rangle}{F_{\mathrm{trop}}{}' - \int_{300}^{P_s} \langle \frac{\partial h_{\mathrm{m}}{}'}{\partial t} \rangle \frac{dp}{g}}, \tag{1}$$

where NSF is the net surface flux (the sum of turbulent energy fluxes and net longwave radiation; positive downward), $F_{\mathrm{trop}}$ is the polar cap–averaged tropospheric MSE flux convergence, and $h_{\mathrm{m}}$ is the moist enthalpy (latent and sensible heat). Angle brackets indicate polar cap–averages and primes indicate anomalies relative to the daily mean annual cycle; $E_{\mathrm{trop}}$ is computed with daily mean anomalies. Note that the contribution from the geopotential energy tendency is not explicitly written in the moist enthalpy tendency term in (1) as the dry enthalpy (sensible heat) accounts for changes in internal and potential energy—a consequence of hydrostatic balance (see Boer 1982). Although the absorbed shortwave flux would typically be included in the NSF term in (1), we neglect it since our analysis is limited to winter.

The denominator in (1), which we refer to as the net tropospheric energy source (NTES), is the net excess energy available after accounting for the moist enthalpy storage in the Arctic atmosphere. The denominator thus represents the maximum energy available for anomalous surface heating. By taking the ratio of the anomalous NSF to NTES, our metric $E_{\mathrm{trop}}$ approximates the fraction of the atmospheric source that heats the surface during periods of anomalously strong $F_{\mathrm{trop}}$. We then assume that the residual fraction $1 - E_{\mathrm{trop}}$ is lost upward due to fluxes across the tropopause. The moist enthalpy tendency is computed using second-order accurate central differences using 3-hourly data and then averaged daily. Contributions from the kinetic energy to NTES are small and have been neglected.

All anomalies have been linearly detrended and a low-pass filter with a 2-day cutoff frequency was applied to NTES anomalies prior to calculation of the metric. The potential impact of unrealistic long-term trends in polar cap–averaged fields in reanalyses (e.g., Taylor et al. 2018) on




Accepted for publication in *Journal of Climate*. DOI 10.1175/JCLI-D-21-0852.1.

$E_{\mathrm{trop}}$ prompted the use of detrended anomalies. Applying a low-pass filter increased the winter correlation between NTES [i.e., denominator of (1)] and the NSF (0.75 to 0.83) and increased the number of winter days with an $E_{\mathrm{trop}}$ between 0 and 1 (an additional 60 days)—indicating a reduction in the energy imbalance.

Figure 1 shows a histogram of $E_{\mathrm{trop}}$ over all winter days. $E_{\mathrm{trop}}$ would be physically bounded between 0 and 1 if atmospheric MSE fluxes were the only potential drivers of anomalous NSF. In reality, the NSF is also dependent on processes internal to the Arctic, and $E_{\mathrm{trop}}$ could become large on days when NTES (denominator) is small. Examples of these internal processes include energy fluxes across the tropopause that are forced by stratospheric processes and strong surface winds that drive sea ice (mechanical forcing) and surface flux changes. $E_{\mathrm{trop}}$ falls between 0 and 1 on 63% of all winter days (not shown). Most days outside this range (i.e., $E_{\mathrm{trop}}$ greater than 1 or less than 0) are associated with small anomalies in NTES. These are days for which the atmosphere would have little potential to drive NSF anomalies. For example, days with an NTES magnitude less than 12 $\mathrm{W\,m^{-2}}$ (approximately the bottom 50% of days) make up 85% of days with an $E_{\mathrm{trop}}$ greater than 1 or less than 0. Additionally, Cardinale et al. (2021) found that energy budget residuals in MERRA-2 are small relative to $F_{\mathrm{trop}}$ and the NSF during periods of anomalously large $F_{\mathrm{trop}}$, increasing our confidence that MERRA-2 provides an accurate $E_{\mathrm{trop}}$ during significant tropospheric heating events.

### *c. Definition of tropospheric energy flux events*

Tropospheric energy flux (i.e., $F_{\mathrm{trop}}$) events on synoptic timescales are identified and assigned a mean $E_{\mathrm{trop}}$ using the following procedure:

1) Isolate days when the NTES anomaly is greater than 0.

2) Calculate the cumulative time integral of the NTES anomaly over each event period—the consecutive days that meet the first criteria.

3) An event is defined as a cumulative increase of 8 $\mathrm{MJ\,m^{-2}}$, with the event date (also referred to as the central date) defined as the day on which the threshold is reached.

4) Calculate the mean $E_{\mathrm{trop}}$ over the event period (including the event date) for days when $E_{\mathrm{trop}}$ is between 0 and 1.





Accepted for publication in *Journal of Climate*. DOI 10.1175/JCLI-D-21-0852.1.

The 8 $\mathrm{MJ\,m^{-2}}$ threshold maximizes the amount of events that are 2–6 days apart [synoptic timescales; Gulev et al. (2002)], while reducing events that occur less than two days apart. Additionally, for all anomalously positive NTES periods, the average cumulative NTES anomaly is about 8 $\mathrm{MJ\,m^{-2}}$.

In contrast to the definition of $F_{\mathrm{trop}}$ events, composite analysis of events with various mean $E_{\mathrm{trop}}$ (section 3b) includes days with an $E_{\mathrm{trop}}$ greater than 1 or less than 0; however, results of this study are not sensitive to this choice. We decide to include these days for better visualization of the temporal and vertical structure of events.

## 3. Surface heating efficiencies of winter tropospheric energy flux events

### *a. High, medium, and low-efficiency events*

Figure 1 shows histograms of both daily $E_{\mathrm{trop}}$ for all winter days and mean $E_{\mathrm{trop}}$ during winter-season synoptic-scale $F_{\mathrm{trop}}$ events as defined in Section 2c. The mean $E_{\mathrm{trop}}$ over the subset of all days with $E_{\mathrm{trop}}$ between 0 and 1 (63% of days) is 50%. This indicates that half of the anomalous net tropospheric energy source (NTES) goes toward anomalous heating of the surface and half is expressed as an upward loss across the tropopause. The separation into three efficiency-based categories (high, medium, and low-efficiency events) is sensible given the approximately normal

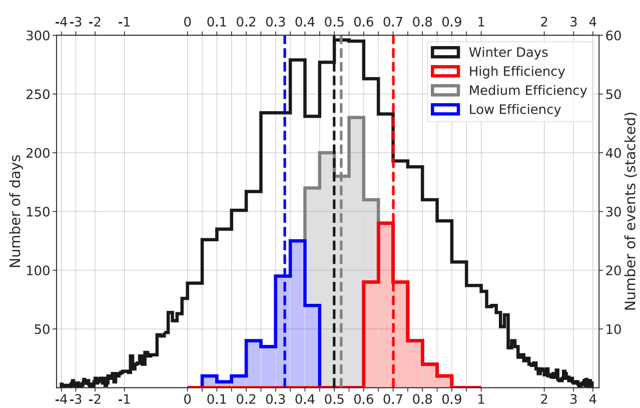


FIG. 1. Daily efficiencies during winter (NDJMF) from January 1980 to March 2020 (black) and time mean efficiencies of high (red), medium (gray), and low (blue) efficiency events. Dashed vertical lines indicate the mean of each distribution, excluding days with an efficiency less than 0 or greater than 1. A linear scale is used between 0 and 1 and a logarithmic scale is used elsewhere.



Accepted for publication in *Journal of Climate*. DOI 10.1175/JCLI-D-21-0852.1.

distribution of the event mean $E_{\mathrm{trop}}$. High and low-efficiency events are defined as events with an average $E_{\mathrm{trop}}$ greater than or equal to the 75th percentile ($E_{\mathrm{trop}} \geq 0.63$) and less than or equal to the 25th percentile ($E_{\mathrm{trop}} \leq 0.42$) of events, respectively. The remainder of the events are classified as medium-efficiency events. These percentiles are calculated from the event mean $E_{\mathrm{trop}}$, not from all days. In total, there are 312 events (7.8 per season), separated into 78 high, 156 medium, and 78 low-efficiency events.

Figure 2 provides an example of the identification of $F_{\mathrm{trop}}$ events and their separation into high, medium, and low-efficiency during the 2009–2010 winter season. Eight total events are identified, with three of these positive NTES periods each containing two events. Multiple events are allowed in the same positive NTES period if the 8 $\mathrm{MJ\,m^{-2}}$ threshold is crossed multiple times (e.g., at 8 and 16 $\mathrm{MJ\,m^{-2}}$). In total, about half of all events occur in multiple event periods; in these periods, there is an average of about 4 days between events. 60, 58, and 32% of high, medium, and low-efficiency events follow another event in the same period (not shown).

The events in Fig. 2 are separated into four high, one medium, and three low-efficiency events indicated by the cumulative average $E_{\mathrm{trop}}$ when a threshold is reached (red, gray, and blue bars in the upper panel of Fig. 2). The mean $E_{\mathrm{trop}}$ of each event can also be seen by comparing NTES with the net surface flux (NSF); events with the highest $E_{\mathrm{trop}}$ are associated with the smallest difference between the time-integrated NTES and NSF. Fig. 2 also shows several episodes of positive NTES that do not meet our 8 $\mathrm{MJ\,m^{-2}}$ threshold and are thus not counted as events. In total, there are 135 episodes that do not meet the 8 $\mathrm{MJ\,m^{-2}}$ threshold; if included, these events would make up about 36% of events.

Anomalies in NTES and $F_{\mathrm{trop}}$ are shown in the lower panel of Fig. 2. Events (i.e., periods of positive NTES anomalies) are typically preceded by positive $F_{\mathrm{trop}}$ anomalies. Distinct positive $F_{\mathrm{trop}}$ anomalies are also typically found before events that are closely preceded by another event (blue lines prior to the second and fourth events in Fig. 2); thus, it is sensible to consider these events as separate. However, some events (e.g., the eighth event in Fig. 2) are associated with neutral or negative $F_{\mathrm{trop}}$ anomalies and the tropospheric forcing is hard to distinguish from the previous event. For example, it appears that a single persistent $F_{\mathrm{trop}}$ anomaly forces both the seventh and eighth events; the troposphere remained anomalously warm and moist long enough for another event to be identified even when coincident with a negative $F_{\mathrm{trop}}$ anomaly.



Accepted for publication in *Journal of Climate*. DOI 10.1175/JCLI-D-21-0852.1.

Figures 1 and 2 reveal that events with similar tropospheric heating can have very different impacts on the surface energy budget. To improve our understanding of the processes that determine $E_{\mathrm{trop}}$ during these events, we compare composites of high, medium, and low-efficiency events. Composited quantities to be analyzed include atmospheric temperatures, sea ice concentration (SIC), lower-tropospheric stability [calculated as the potential temperature ($\theta$) difference between 850 hPa and 2-m; $\theta_{850\mathrm{hPa}} - \theta_{2\mathrm{m}}$], surface fluxes, local MSE flux convergence, and cloud concentrations in the 30 days before and after the central dates of events. For events that occur in November and March, the composite analysis includes some days in October and April. Results from the composite analysis in section 3b will mainly be provided in three periods: "before" (day −21 to −7), "during" (day −7 to 7), and "after" (day 7 to 21) the event. Based on the method for defining events described above, the maximum anomalous NTES occurs in the "during" period.

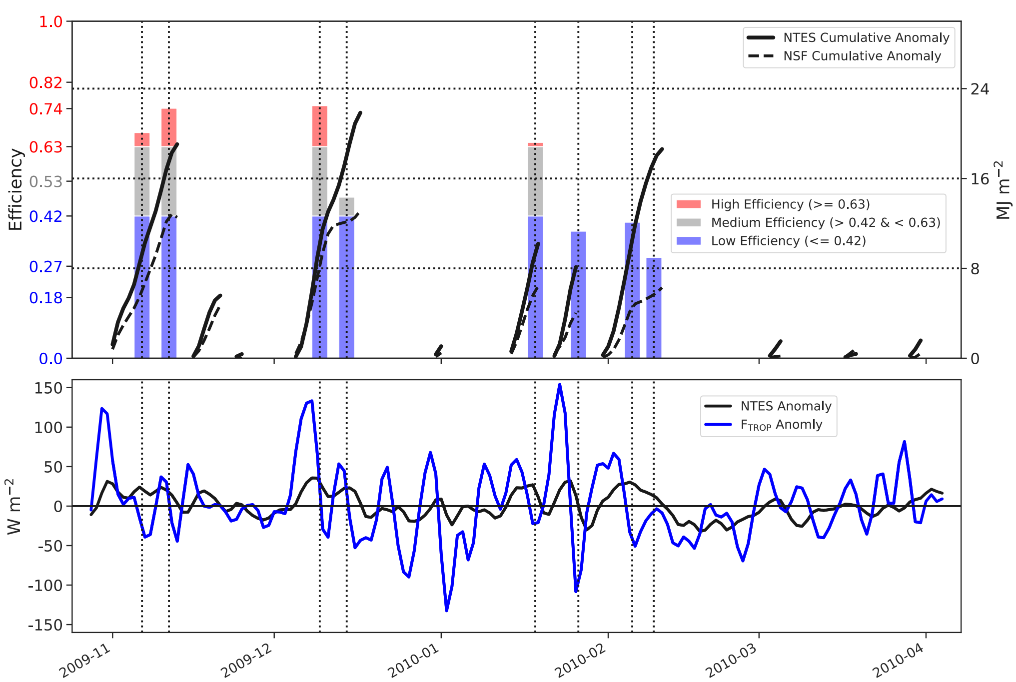


FIG. 2. (Upper) Cumulative time integrals of anomalies in the net tropospheric energy source (NTES; solid black; MJ m$^{-2}$) and net surface flux (dashed black; MJ m$^{-2}$) and the event mean efficiency ($E_{\mathrm{trop}}$; bars) for each event during the 2009–2010 winter season. Dotted vertical lines indicate central dates of high (red bars), medium (gray bars) and low (blue bars) efficiency events and dotted horizontal lines indicate event thresholds. (Lower) Anomalies in $F_{\mathrm{trop}}$ (blue; W m$^{-2}$) and NTES (black; W m$^{-2}$) during the 2009–2010 winter season.



Accepted for publication in *Journal of Climate*. DOI 10.1175/JCLI-D-21-0852.1.

The anomalous poleward MSE flux convergence, on the other hand, does not neatly fit into the "before" or "during" period as it tends to span days −14 to 0.

### b. Event Comparisons

#### 1) Before events—preconditioning

Figure 3 shows the polar cap–averaged and Atlantic sector–averaged (20°W to 80°E) anomalies in the 2-m temperature and SIC for high, medium, and low-efficiency events. The Atlantic sector average is provided, as this region is generally associated with the largest anomalies. High-efficiency events are found to have a different preconditioning of the Arctic surface than medium and low-efficiency events; these differences are statistically significant mainly in the Atlantic sector (cf. dashed lines in Figs. 3a–c). In the high-efficiency composite prior to day −7 (i.e., prior to the onset of anomalous surface heating), 2-m temperature anomalies are positive and SIC anomalies are negative, especially in the Atlantic sector. In the same period for both medium and low-efficiency composites, Atlantic sector 2-m temperature and SIC anomalies are generally negative and positive, respectively. The statistically significant differences between events are not largely explained by the presence of antecedent events. The preconditioning signal is qualitatively similar in event composites that require events to be at least 21 days apart (not shown).

Figures 4a–c show spatial maps of SIC anomalies and lower-tropospheric stability anomalies during the "before" period. The largest SIC anomalies excluding the Canadian Archipelago are found in the Barents–Kara Seas. In the high-efficiency composite, decreased stability is found over the majority of the Arctic Ocean, with the largest negative anomalies found over areas of negative SIC anomalies (Fig. 4a), suggesting increased lower-tropospheric turbulent mixing. In the medium and low-efficiency composites, increased stability is found over much of the Arctic Ocean, especially over areas of increased SIC anomalies (Figs. 4b and 4c), suggesting decreased lower-tropospheric turbulent mixing. The association between stability and SIC anomalies is consistent with Deser et al. (2010) and Vihma (2014); enhanced turbulent heat fluxes are found in areas of reduced SIC and act to warm the air above the surface and decrease the stability of the lower troposphere, while suppressed turbulent heat fluxes are found in areas of increased SIC and act to increase the stability (not shown).



Accepted for publication in *Journal of Climate*. DOI 10.1175/JCLI-D-21-0852.1.

The vertical structure of anomalous atmospheric temperatures in the polar cap average before day −7 (Figs. 5a–c) reveal that temperature anomalies extend the depth of the troposphere. Polar cap–averaged lower-tropospheric stability anomalies are negative and positive in high and medium-efficiency events, respectively, consistent with anomalies in the Barents–Kara Seas (Figs. 4a and 4b). Low-efficiency events are associated with the lowest tropospheric temperatures; however, polar cap–averaged stability anomalies are negative (reduced) mainly due to contributions from the Canadian Archipelago (Fig. 4c).

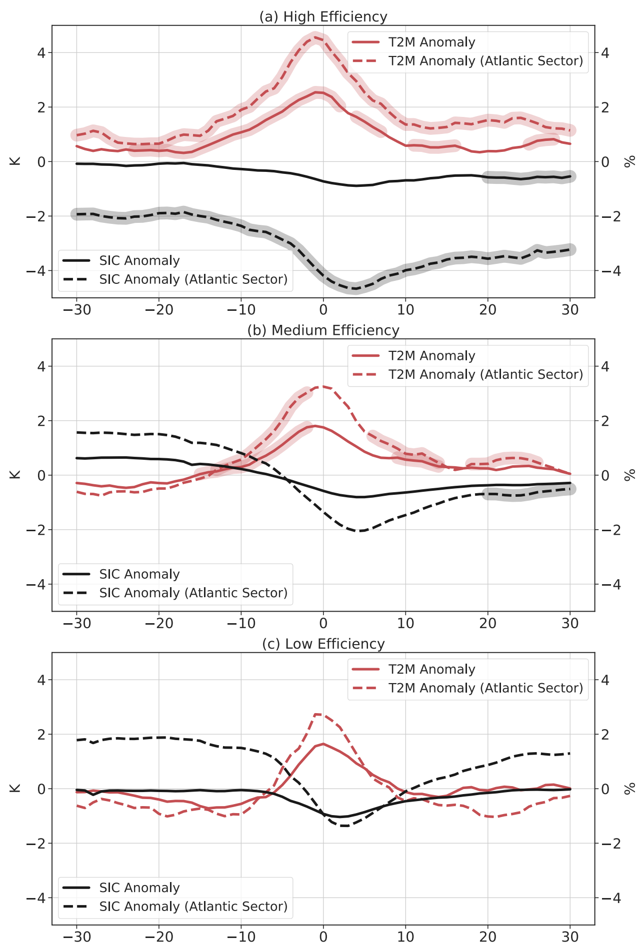


FIG. 3. Composite of polar cap–averaged (solid) and Atlantic sector–averaged (dashed) anomalies in 2-m temperature (K; red) and sea ice concentration (%; black) in the 30 days before and after the central date of (a) high, (b) medium, and (c) low-efficiency events. The shading indicates anomalies statistically different from low-efficiency events at the 95% confidence level. A two-sided $t$-test was used to determine significance. For $p$ values < 0.05, we reject the null hypothesis of equal averages.



Accepted for publication in *Journal of Climate*. DOI 10.1175/JCLI-D-21-0852.1.

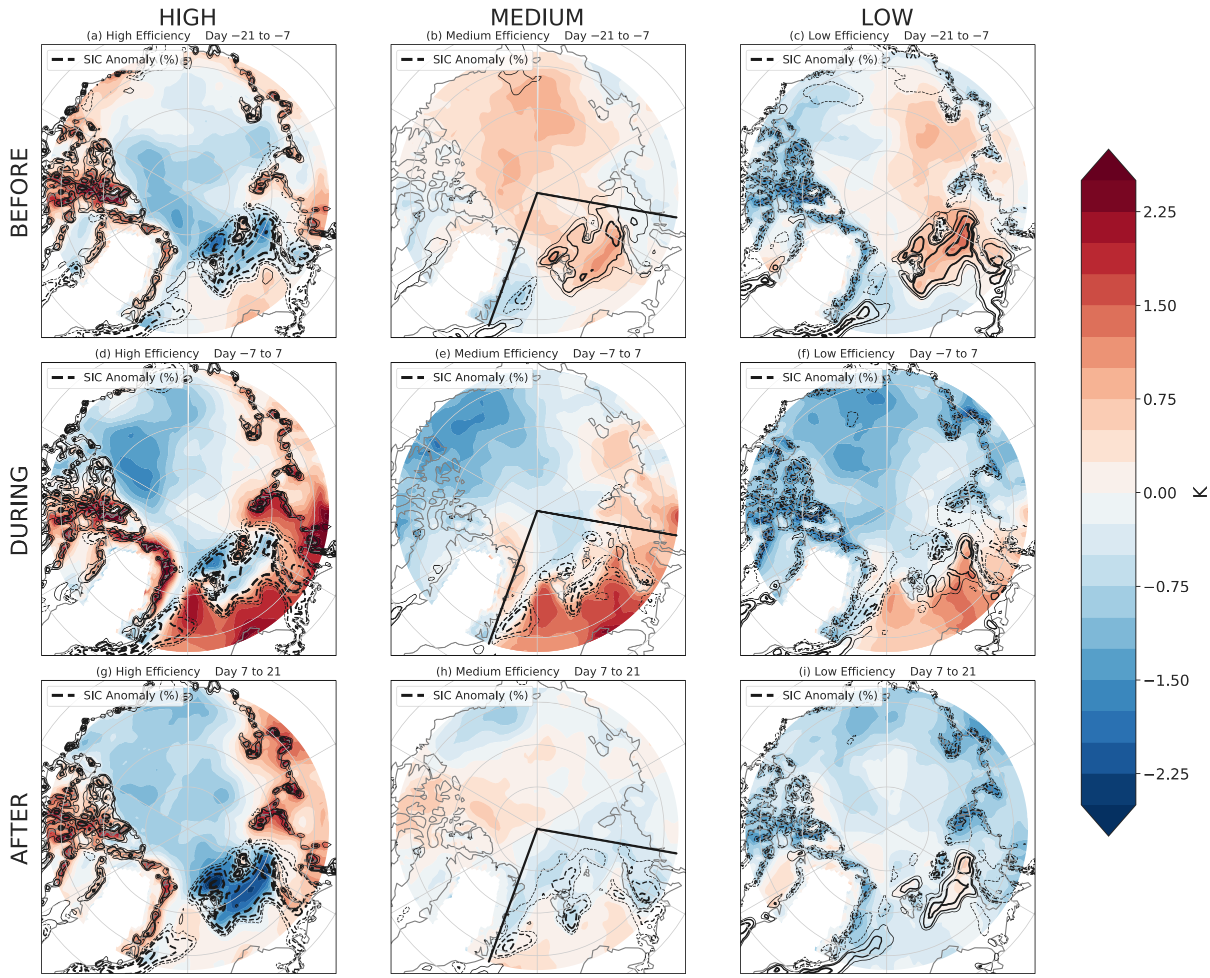


FIG. 4. Composite of anomalous time mean lower-tropospheric stability (K, fill) and sea ice concentration (%, SIC; black contours) during the period (a)–(c) before (day −21 to −7), (d)–(f) during (day −7 to 7), and (g)–(i) after (day 7 to 21) the central date of (left) high, (center) medium, and (right) low-efficiency events. SIC anomalies are contoured at 1.5, 3, 6, 12, and 24%, with line widths increasing with magnitude. Solid and dashed contours indicate positive and negative SIC anomalies, respectively. The boundaries of the Atlantic sector (20°W to 80°E and 70°N to 90°N) are also shown (black longitude lines) in (b), (e), and (h).

### 2) DURING EVENTS

Figure 5 includes composites of the vertical and temporal structure of polar cap–averaged temperature anomalies (Figs. 5a–c) and the cumulative time integral of anomalous local MSE flux convergence (filled contours in Figs. 5d–f). The use of cumulative time integrals allows for easier visualization of the vertical structure of the flux anomalies and comparison with the



Accepted for publication in *Journal of Climate*. DOI 10.1175/JCLI-D-21-0852.1.

temperature anomalies. Positive anomalies in the MSE flux convergence—which increase the sensible and latent energy of the Arctic column—emerge at approximately day $-14$ in all three composites. MSE flux convergence anomalies have a similar "bottom-heavy" profile in high and medium-efficiency events; anomalies maximize in the lower troposphere and increase with pressure until around 925 hPa (Figs. 5d and 5e). The MSE flux convergence anomalies in low-efficiency events are approximately vertically uniform above 925 hPa (Fig. 5f). In all three composites, the sensible (SH) and latent (LH) flux convergence anomalies maximized in the lower troposphere are compensated by geopotential (GP) flux divergence (negative) anomalies (cf. red and black contours in Figs. 5d–f). The lack of a bottom-heavy MSE flux convergence in the low-efficiency composite results from a weaker vertical gradient in positive SH and LH flux anomalies and stronger negative anomalies in the GP flux that extend deeper into the troposphere. Additionally, the near-surface layer of anomalous MSE flux divergence decreases in depth and intensity from low to high-efficiency (cf. brown-filled contours between events in Figs. 5d–f). Despite vertical structure differences, the cumulative $F_{\mathrm{trop}}$ anomaly at day 0 is similar for each event composite, with values of 28.9, 26.2, and 24.5 MJ $\mathrm{m}^{-2}$ in high, medium, and low-efficiency events, respectively (blue lines in Figs. 5g–i).

The vertical structure of anomalous warming in high, medium, and low-efficiency events can be explained by considering the vertical structure of the MSE convergence and the lower-tropospheric stability. The vertical structure of the flux convergence compares reasonably well with the warming structure (cf. red-filled contours in Figs. 5a–c and green-filled contours in Figs. 5d–f). Despite similarities in the flux convergence in high and medium-efficiency events, high-efficiency events are associated with larger lower-tropospheric temperature anomalies. High-efficiency events occur in the presence of reduced Atlantic sector SIC, which reduces the lower-tropospheric stability and increases turbulent mixing (Fig. 4a)—likely enhancing the lower-tropospheric temperature anomaly by mixing the heating anomaly to the surface (Kayser et al. 2017). Both medium and low-efficiency events occur in the presence of enhanced Atlantic sector SIC, which increases the lower-tropospheric stability and decreases turbulent mixing (Figs. 4b and 4c); thus, differences in lower-tropospheric temperature anomalies between medium and low-efficiency events can be explained by differences in the vertical structure of the MSE convergence. From a Lagrangian perspective, as anomalously warm and moist air propagates through a stratified Arctic, it ascends



Accepted for publication in *Journal of Climate*. DOI 10.1175/JCLI-D-21-0852.1.

along or slightly less than the slope of isentropic surfaces (Komatsu et al. 2018; You et al. 2021).

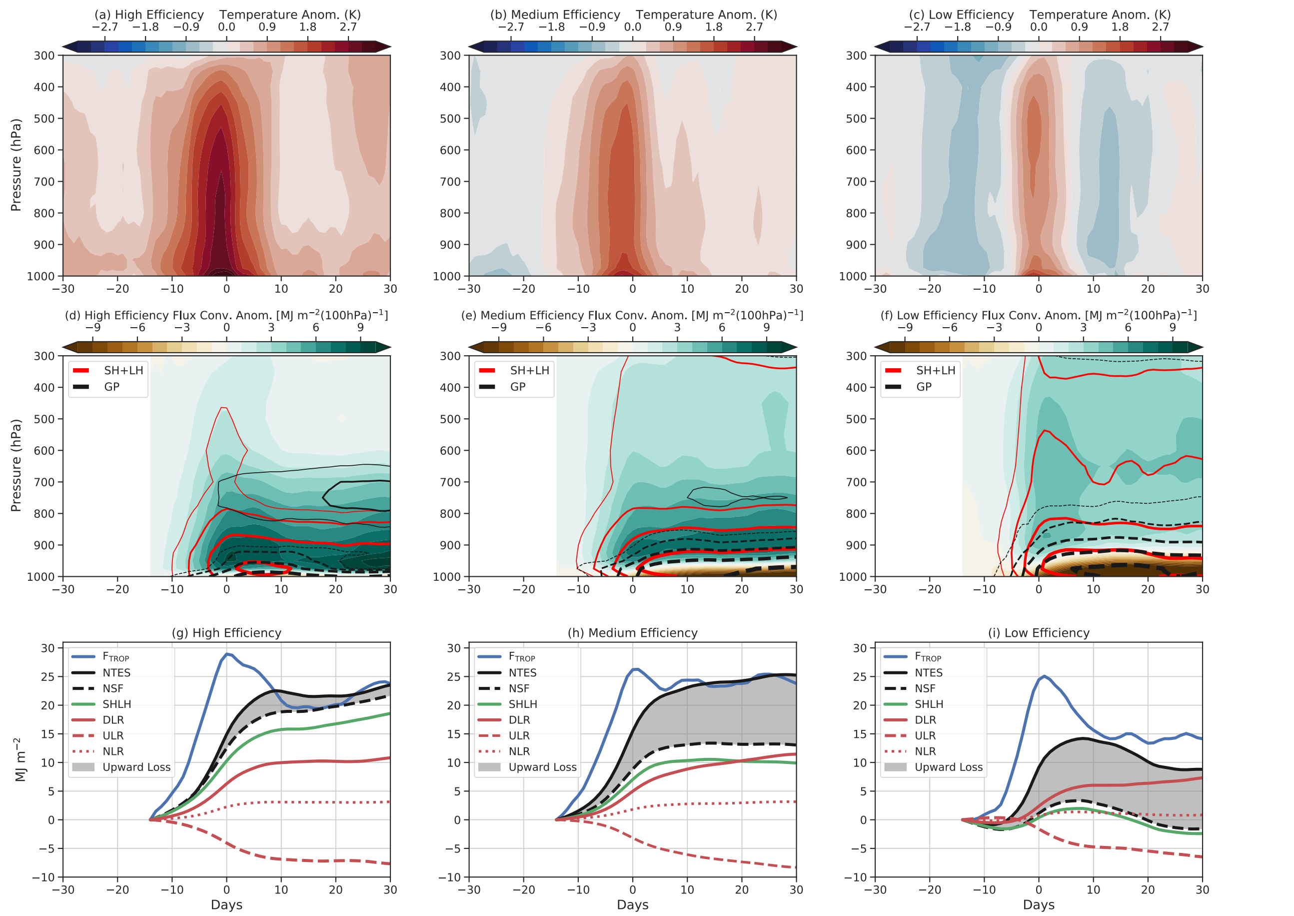


FIG. 5. Composite of the (a)–(c) polar cap–averaged anomalous temperature (K), (d)–(f) cumulative time integral of the anomalous local MSE flux convergence poleward of 70°N [fill; $\mathrm{W\,m^{-2}\,(100hPa)^{-1}}$] and contributions from the combined SH and LH components (red) and the GP component (black) during (left) high, (center) medium, and (right) low-efficiency events. The SH, LH, and GP anomalies in (d)–(f) are contoured at 2, 4, 8, 16, and 32 $\mathrm{W\,m^{-2}\,(100hPa)^{-1}}$, with line widths increasing with magnitude. Solid and dashed contours indicate positive and negative anomalies, respectively. (g)–(i) show cumulative anomalies in $F_{\mathrm{trop}}$ (blue), the net tropospheric energy source (NTES; solid black), and net surface flux (NSF; dashed black). NSF anomalies (positive downward) are decomposed into additive contributions from sensible and latent surface turbulent heat fluxes (SHLH; green) and net longwave radiation flux (NLR; dotted red). NLR is further decomposed into anomalous upward (ULR; dashed red) and downward (DLR; solid red) fluxes. The gray shading shows the residual between the NTES and NSF, which we interpret as upward loss.



Accepted for publication in *Journal of Climate*. DOI 10.1175/JCLI-D-21-0852.1.

In a relatively unstratified Arctic (e.g., high-efficiency events), the anomalously warm and moist air may remain closer and better coupled to the surface.

Figure 5 also includes composites of cumulative time integrals of anomalous NTES and polar cap–averaged fluxes at the surface and tropopause. NTES and NSF begin to increase 1–2 weeks before the central date and peak 1–2 weeks after the central date. The interpretation that an NSF anomaly represents the fraction of an NTES anomaly that heats the surface should be approximately valid during these events in which $F_{\mathrm{trop}}$ is anomalously large. In low-efficiency events, the NTES anomaly only becomes positive when the troposphere is anomalously warm and moist, around day −5 (black line in Fig. 5i). The noticeably smaller peak in the anomalous NTES in the low-efficiency composite mainly results from a larger fraction of the $F_{\mathrm{trop}}$ anomaly going into moist enthalpy storage (not shown) and a shorter duration of positive temperature anomalies (cf. red-filled contours between events in Figs. 5a–c). Only a small increase in the downward (DLR) and net (NLR) longwave fluxes are found when moving from low to high-efficiency (cf. red lines in Figs. 5g–i). Differences in the NSF and $E_{\mathrm{trop}}$ between events, visualized by the size of the shaded residual, are best explained by differences in the combined sensible and latent turbulent heat (SHLH) fluxes (cf. green lines). This suggests that near-surface warming and moistening over areas of open ocean or thin sea ice are key to reducing surface heat loss (i.e., positive NSF anomalies) and increasing $E_{\mathrm{trop}}$. Additionally, the SHLH term is the dominant contributor to the anomalous polar cap–averaged NSF in high and medium-efficiency events from day −14 to 10. These results appear inconsistent with Chen et al. (2018), who suggested that turbulent heat fluxes play a secondary role in synoptic-scale events; however, their study mainly focused on sea ice variability and did not include areas of majority exposed ocean.

To investigate further the mechanisms determining $E_{\mathrm{trop}}$, we show in Fig. 6 the time-integrated polar cap–averaged anomalies in surface fluxes and the upward loss from day −14 to 10 for each event composite. These values are identical to those shown for day 10 in Figs. 5g–i. Also shown are contributions to the Arctic average from areas of open ocean (SIC < 15%; i.e., the ice edge), partial sea ice (98% > SIC > 15%), and the combined areas of nearly full ice cover (SIC > 98%) and land. In all events, SHLH anomalies are the dominant contributor to the anomalous NSF in areas of open ocean, while DLR is the dominant contributor to the anomalous NSF over sea ice and land, consistent with Woods and Caballero (2016). However, differences in the anomalous





Accepted for publication in *Journal of Climate*. DOI 10.1175/JCLI-D-21-0852.1.

NSF, and thus $E_{trop}$, between events are best explained by SHLH anomalies in the Arctic average, areas of open ocean, and areas of partial sea ice up to 98% SIC (cf. green boxes between events). Changes in SHLH anomalies between events over areas of open ocean and partial sea ice appear of equal importance. Interestingly, downward SHLH anomalies in high-efficiency events in areas of partial ice cover result in part from increased SIC anomalies in the Canadian Archipelago, while the upward SHLH anomalies in low-efficiency events result in part from decreased SIC in the Canadian Archipelago (not shown). Changes in DLR anomalies between events are only dominant in areas with near 100% SIC and land, where absolute contributions to the polar cap–averaged NSF are relatively small. Additionally, when normalized by the time-integrated NTES anomaly from day −14 to 10, polar cap–averaged DLR anomalies are approximately equal in all three events and NLR anomalies only slightly increase from low to high-efficiency (not shown). During this period, longwave fluxes only contribute 8% of the change in $E_{trop}$.

The relatively large downward SHLH anomalies in high and medium-efficiency events in areas of open ocean and partial sea ice have implications for Atlantic water temperatures and sea ice growth, respectively. However, there exist substantial uncertainties in SHLH over areas of sea ice (e.g., Taylor et al. 2018; Graham et al. 2019a), especially during cold-stable periods in winter, where upward SHLH biases are found (Graham et al. 2019a). Although these biases are largely explained by differences in point observations and grid cell averages which contain a fraction of open ocean, upward biases are still found when compared to satellite-retrieved SHLH. Satellite-retrieved climatological SHLH is downward (i.e., the surface acts as an atmospheric heat sink) during winter over areas of sea ice (Taylor et al. 2018), while the climatological winter SHLH is weakly upward in MERRA-2 (not shown). Errors in SHLH should then be smaller in the warm periods associated with $F_{trop}$ events; however, relative to the climatologically downward satellite-retrieved SHLH over sea ice, SHLH anomalies over sea ice (Fig. 6) would be reduced. These uncertainties would not greatly impact surface flux differences between events, assuming that the potential biases are equal in all events.

Figure 7 shows the zonal structure of the anomalous local MSE flux convergence and contributions from eddy, mean meridional circulation (MMC), and LH fluxes in the 14 day average before the central date of events. The majority of tropospheric heating in all three events can be attributed to eddy fluxes, dominated by SH and LH fluxes (not shown), consistent with past work (e.g., Yoo et al.



Accepted for publication in *Journal of Climate*. DOI 10.1175/JCLI-D-21-0852.1.

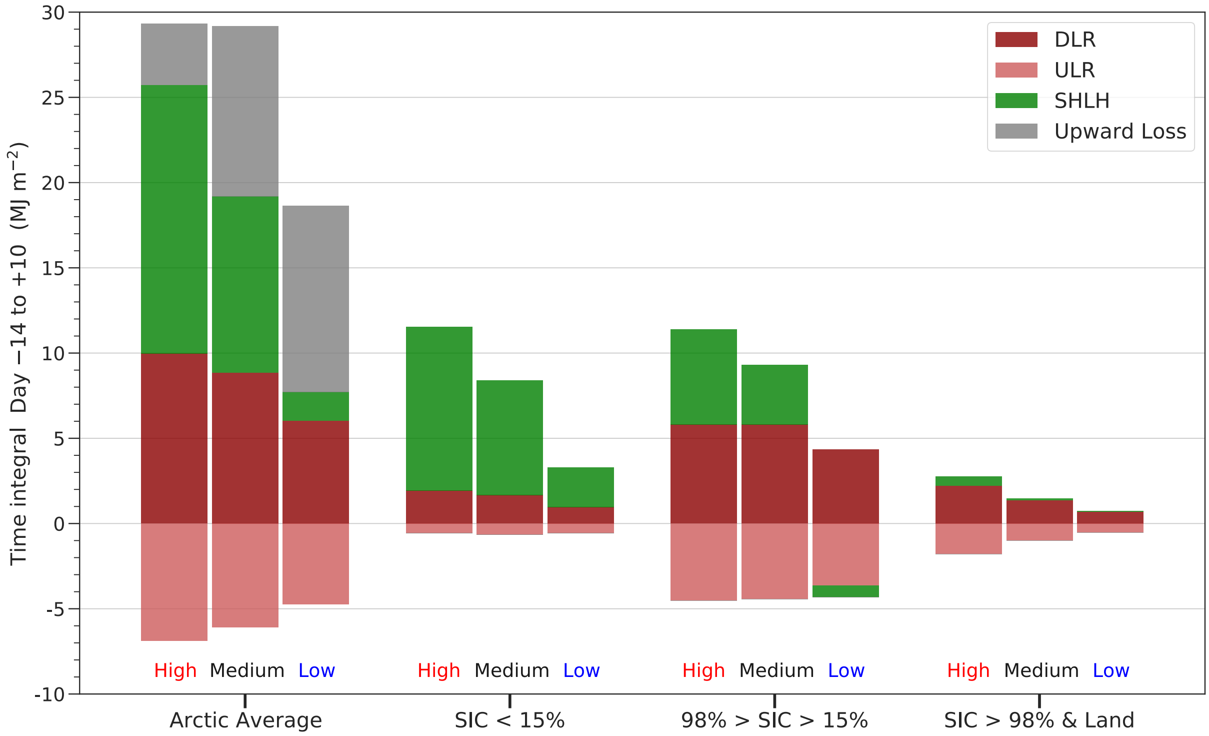


FIG. 6. Time-integrated anomalies (MJ m$^{-2}$) in the polar cap–averaged DLR (dark red boxes), SHLH (green boxes), upward loss (gray boxes), and ULR (light red boxes) from day −14 to 10 in high, medium, and low-efficiency events. Also shown are absolute contributions to the polar cap–averaged NSF in areas of SIC < 15% (open ocean), 98% > SIC > 15%, and SIC > 98% and land. Polar cap–averaged anomalies are identical to the anomalies in (g)–(i) of Fig. 5 at day 10.

2012; Baggett and Lee 2015, 2017). In high and medium-efficiency events, the local MSE flux convergence is concentrated in the Atlantic sector (Figs. 7a and 7c), much like the moist intrusion events in Woods and Caballero (2016), with a more zonally uniform flux in low-efficiency events (Fig. 7e). Negative MMC anomalies—dominated by GP fluxes (not shown)—indicate adiabatic cooling and act to cool the lower troposphere, especially in low-efficiency events (solid blue lines in Figs. 7b, 7d, and 7f). Positive contributions from the LH and SH components to the MMC flux indicate warm and moist inflow and partially compensate the adiabatic cooling (not shown). In high-efficiency events, positive anomalies in the lower-tropospheric MMC prior to day −14 (not shown) may also help explain the warm troposphere prior to the event—consistent with adiabatic warming preceding eddy fluxes during Arctic surface warming events initiated by tropical convection (Yoo et al. 2012). Lower-tropospheric MSE flux convergence anomalies in high and



Accepted for publication in *Journal of Climate*. DOI 10.1175/JCLI-D-21-0852.1.

medium-efficiency events are significantly different from low-efficiency events (thick black lines in Figs. 7b and 7d) due to enhanced positive eddy flux anomalies and reduced negative MMC flux anomalies. All three events are associated with poleward LH flux anomalies, with a significant difference between high and low-efficiency events. However, increases in the LH flux from low to high-efficiency are small relative to increases in the total MSE flux (cf. solid and dashed black lines in Figs. 7b, 7d, and 7f) and only partially explain differences in lower-tropospheric and surface heating between events.

The 2-m temperature and SIC responses shown in Fig. 3 are consistent with the anomalous surface fluxes and zonal structure of each event. The increase in the Atlantic sector 2-m temperatures and the decrease in the Atlantic sector SIC in each event composite is larger than in the polar cap–average, especially in high-efficiency events (cf. dashed and solid lines in Fig. 3a). Although the temperature and SIC tendencies are similar between events, the magnitude and duration of anomalous 2-m temperature and SIC in the Atlantic sector increase from low to high-efficiency. In all composites, lower-tropospheric stability anomalies are largely positive over areas of open ocean in the Atlantic sector (equatorward of SIC anomalies in the Barents–Kara Seas) and negative elsewhere over the Arctic basin (Figs. 4d–f). Relatively large downward SHLH anomalies over areas of open ocean act to slow the near-surface warming relative to 850 hPa, resulting in positive stability anomalies. Large differences in anomalous SIC in the Barents–Kara Seas can be seen in Figs. 4d–f, with relatively large negative anomalies in high, small negative anomalies in medium, and a mix of small negative and positive anomalies in low-efficiency events. Differences in the surface response to each type of event are not due to differences in total energy input into the Arctic column; for example, these results are nearly identical when normalized by the cumulative $F_{\mathrm{trop}}$ from day $-14$ to 0 (not shown).

The cloud response is shown in Fig. 8. In all three event composites, high cloud fraction anomalies are generally positive, especially in the Atlantic sector (Figs. 8g–i). Differences between composites are apparent in middle and low clouds. Mainly negative cloud fraction anomalies are found in the middle and low cloud layers in high-efficiency events, a mix of positive and negative anomalies are found in medium-efficiency events, and mainly positive anomalies are found in low-efficiency events, except for low cloud anomalies in the Atlantic sector (Figs. 8a–c). The results for high and medium-efficiency events are inconsistent with Johansson et al. (2017), who



Accepted for publication in *Journal of Climate*. DOI 10.1175/JCLI-D-21-0852.1.

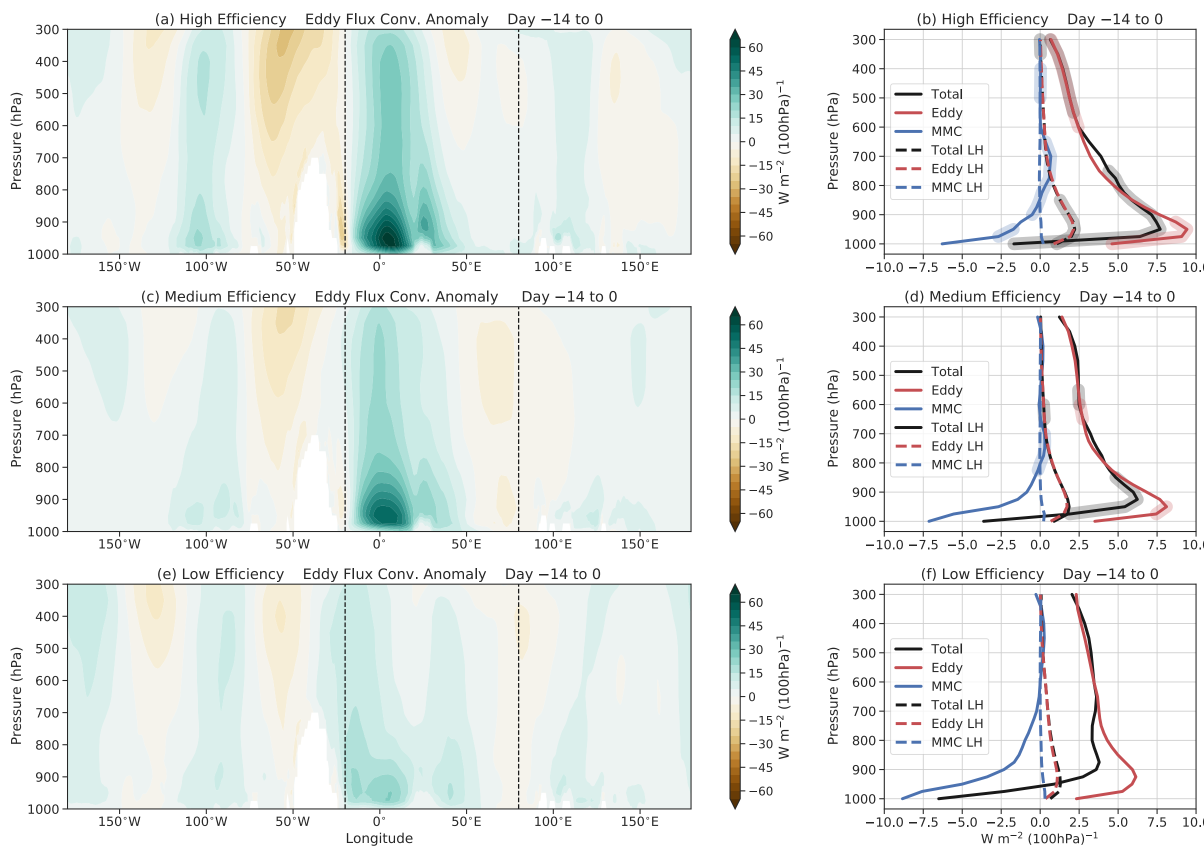


FIG. 7. Composite of the (left) time mean eddy contribution to the local MSE flux convergence and (right) time and zonal mean total local MSE flux convergence (black), with contributions from the eddy (red) mean meridional circulation (MMC; blue), total latent heat (LH; dashed black), eddy LH (dashed red), and MMC LH (dashed blue) fluxes [W m$^{-2}$ (100hPa)$^{-1}$] in the 14 days before the central date of (a)–(b) high, (c)–(d) medium, (e)–(f) low-efficiency events. Vertical dashed lines in (a), (c), and (e) indicate the longitude boundaries of the Atlantic sector (20°W to 80°E). The shading in (b), (d), and (f) indicates anomalies statistically different from low-efficiency events at the 95% confidence level. A two-sided $t$-test was used to determine significance. For $p$ values < 0.05, we reject the null hypothesis of equal averages.

found increased satellite-retrieved cloud fraction anomalies throughout the column during moist intrusions. Additionally, recent studies using satellite data find that reduced lower-tropospheric stability results in increased low cloud amounts (Barton et al. 2012; Solomon et al. 2011, 2014; Taylor et al. 2015; Yu et al. 2019). However, the negative lower-tropospheric stability anomalies over much of the Arctic in all events (Fig. 4a–f) only appear associated with positive cloud anomalies in low-efficiency events. Low cloud amount decreases in high and medium-efficiency



Accepted for publication in *Journal of Climate*. DOI 10.1175/JCLI-D-21-0852.1.

events potentially result from areas of increased stability in the Atlantic sector and over land, or from errors that result from the parameterization of cloud physics in MERRA-2 (Graham et al. 2019a). The decrease in the Atlantic sector low cloud fractions, especially in high-efficiency events, may also result from strong heating in the boundary layer, which raises the inversion level and breaks up stratocumulus clouds (Eirund et al. 2020).

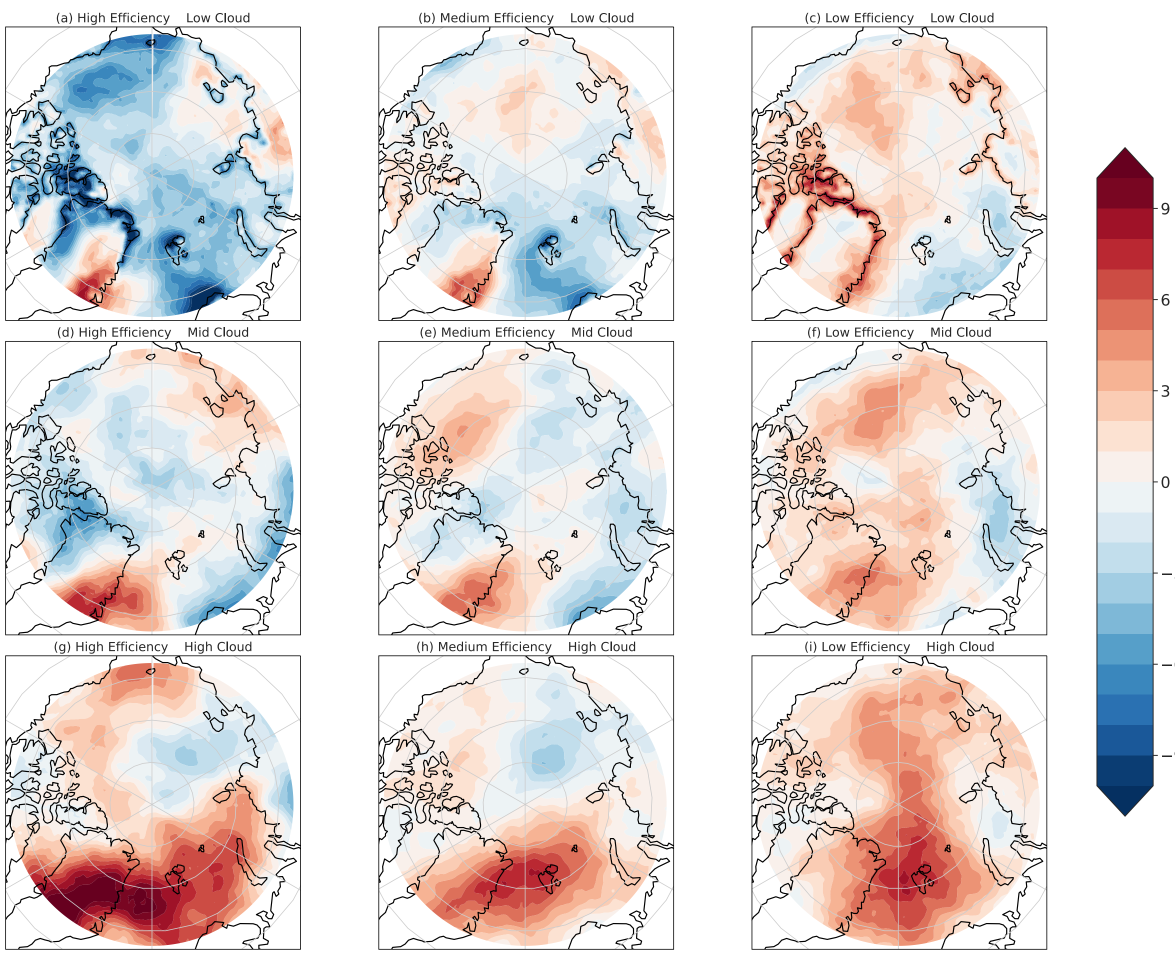


FIG. 8. Composite of time mean (a)–(c) low cloud (below roughly 700 hPa), (d)–(f) middle cloud (about 700–400 hPa), and (g)–(i) high cloud (above about 400 hPa) anomalies (%) during the 7 days before and after the central date of (left) high, (center) medium, and (right) low-efficiency events.

Figure 9 shows the variability in anomalous polar cap–averaged cloud fraction, top-of-atmosphere (TOA) and surface cloud radiative effects (CRE), and surface fluxes. As suggested by the spatial plots, polar cap–averaged cloud fraction anomalies are generally positive, with negative anomalies found in low and middle clouds in high-efficiency events. The relatively weak anomalous TOA



Accepted for publication in *Journal of Climate*. DOI 10.1175/JCLI-D-21-0852.1.

($OLR_{\text{clear-sky}}-OLR$) and surface ($NLR-NLR_{\text{clear-sky}}$) CRE compared to DLR suggests that anomalous cloud fractions do not play an important role in determining $E_{\text{trop}}$. This result is consistent with Sokolowsky et al. (2020), who found that temperature and water vapor impact DLR more than clouds during moist intrusion events over Utqiaġvik, Alaska. The mean CRE in high and medium-efficiency events are close to 0, likely the result of opposing cloud fraction anomalies in lower and upper levels. Additionally, the CRE decreases from low to high-efficiency, acting in the opposite direction of DLR. Figure 9 clearly shows that the variability in the NSF in each event and differences in the NSF between events are best explained by turbulent, not longwave fluxes. High and medium-efficiency SHLH anomalies are statistically different from low-efficiency events at the 95% confidence level. High-efficiency DLR anomalies are also significantly different from low-efficiency events; however, no significant difference is found when anomalies are normalized by the cumulative $F_{\text{trop}}$ anomaly at day 0.

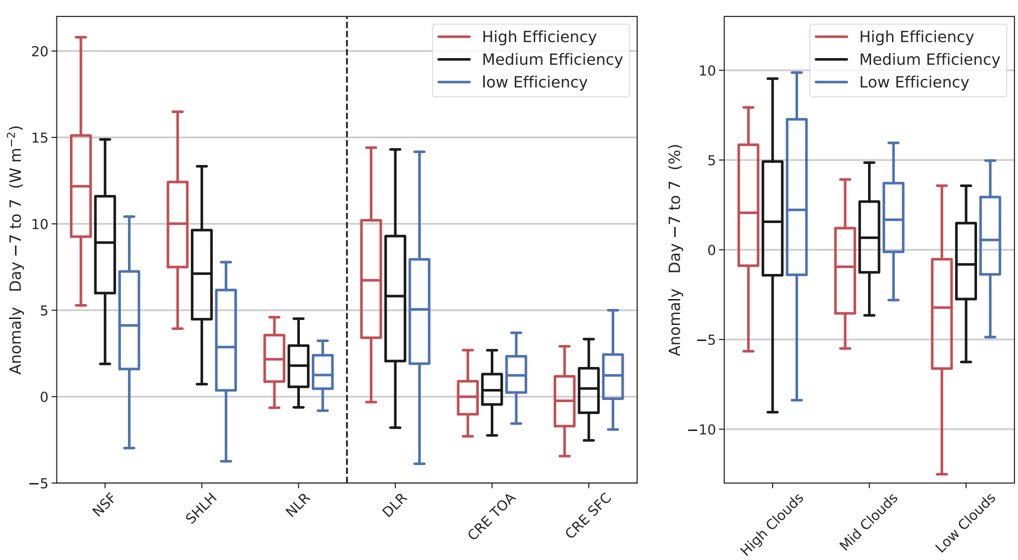


FIG. 9. Box-and-whisker plots of time and polar cap–averaged (left) anomalous ($W\,m^{-2}$) net surface flux (NSF), with contributions from the combined sensible and latent surface turbulent energy fluxes (SHLH) and net longwave flux (NLR), downward longwave flux (DLR) and the cloud radiative effect (CRE) at the top-of-atmosphere (TOA) and surface (SFC), and (right) anomalous high, medium, and low clouds (%) in the 7 days before and after the central date of high (red), medium (black), and low (blue) efficiency events. All boxes extend from the 25th to 75th percentile, with a horizontal line at the mean, and whiskers extend to the 5th and 95th percentiles.



Accepted for publication in Journal of Climate. DOI 10.1175/JCLI-D-21-0852.1.

### 3) After events

We now discuss impacts on the Arctic surface after day 7 (following the passage of the tropospheric heating event), with emphasis on sea ice recovery. Figure 3 shows that in all composites, 2-m temperatures are generally higher and the SIC is generally smaller when compared to the "before" period. SIC anomalies in Figs. 3 and 4 reveal a slower sea ice recovery in both the polar cap average and Atlantic sector average when moving from low to high-efficiency. The slow growth of sea ice following a high-efficiency event is consistent with positive 2-m temperature anomalies (Fig. 3a) that further suppress upward turbulent heat fluxes (Fig. 5g). Near climatological 2-m temperatures in medium-efficiency events are associated with faster sea ice growth relative to high-efficiency events. Negative 2-m temperature anomalies in the Atlantic sector in low-efficiency events are associated with a sea ice growth rate almost equal to the sea ice decline rate during the event—consistent with large negative daily mean SHLH anomalies after day 7 (slope of the green line in Fig. 5i).

After each event, lower-tropospheric stability anomalies generally decrease over the Arctic Ocean (especially in the Atlantic sector), consistent with Johansson et al. (2017) and Liu et al. (2018), associated with decreased SIC anomalies (Figs. 4g–i). Reduced stability over the Barents–Kara Seas is particularly apparent in the high-efficiency composite (Fig. 4g) and is associated with upward anomalies in SHLH in this region (not shown), a likely source for the positive 2-m temperature anomalies over the Arctic during this period—despite downward SHLH anomalies in the polar cap–average.

In Fig. 10, we summarize our understanding of the key distinguishing features of high, medium, and low-efficiency events in the periods "before", "during", and "after" an event. We will use this schematic to anchor a comprehensive discussion in section 4. First, however, we will look at trends in the MERRA-2 data.

## *c. Trends in the efficiency of tropospheric energy flux events*

In section 3, we separated synoptic-scale $F_{\text{trop}}$ events during winter into three efficiency-based categories and found that Arctic surface warming and sea ice loss are indeed larger in events with a higher $E_{\text{trop}}$, despite similar magnitudes of atmospheric forcing (i.e., $F_{\text{trop}}$). Trends in the relative





Accepted for publication in *Journal of Climate*. DOI 10.1175/JCLI-D-21-0852.1.

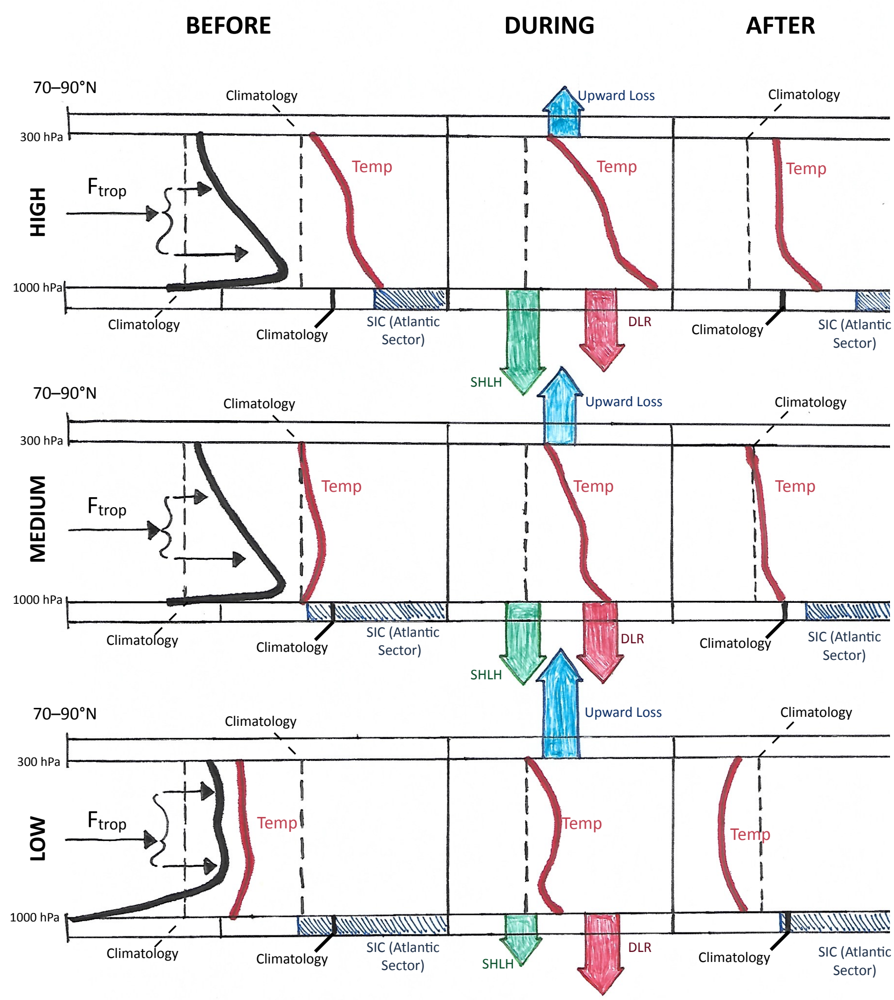


FIG. 10. Schematic of the anomalous energy flux convergence (black), temperature (red), Atlantic sector sea ice concentration (SIC; blue hashed), combined surface sensible and latent turbulent heat flux (green arrows), surface downward longwave flux (red arrows), and upward loss at the tropopause (blue arrows) during the period before, during, and after the central date of (upper) high, (middle) medium, and (lower) low-efficiency events.



Accepted for publication in *Journal of Climate*. DOI 10.1175/JCLI-D-21-0852.1.

frequency of high, medium, and low-efficiency events should then be crucial in understanding the role of synoptic-scale events in Arctic winter warming and sea ice decline.

Figure 11 shows the cumulative sum of seasonal (winter) high, medium, and low-efficiency events from January 1980 to March 2020. Over the last two decades, the number of high-efficiency events has rapidly increased, while low-efficiency event frequency has declined. High-efficiency events have increased by about two events per year and low-efficiency events have decreased by about two events per year, with little change in the frequency of medium-efficiency events, as indicated by the decadal changes in the average number of events per year in Fig. 11. In general, the increase in high-efficiency events occurs in mid-winter (December–February), while the decrease in low-efficiency events occurs in the middle to late winter (January–March). Although the number of total events remains unchanged throughout the period, the surface heating efficiency of $F_{\mathrm{trop}}$ events has increased.

It is important to note that we linearly detrended the source data prior to computing $E_{\mathrm{trop}}$, but that these trends in counts of events in each efficiency bin are nonetheless evident in Fig. 11. The raw MERRA-2 data actually contain a decreasing $F_{\mathrm{trop}}$ trend and increasing NSF trend; thus, our results based on the detrended data may represent an underestimate of the true $E_{\mathrm{trop}}$ trends. We return to this point in the discussion. Additionally, the event count trends are not sensitive to the method of trend removal from NTES and NSF anomalies (e.g., a removal of the 5-year running mean; not shown).

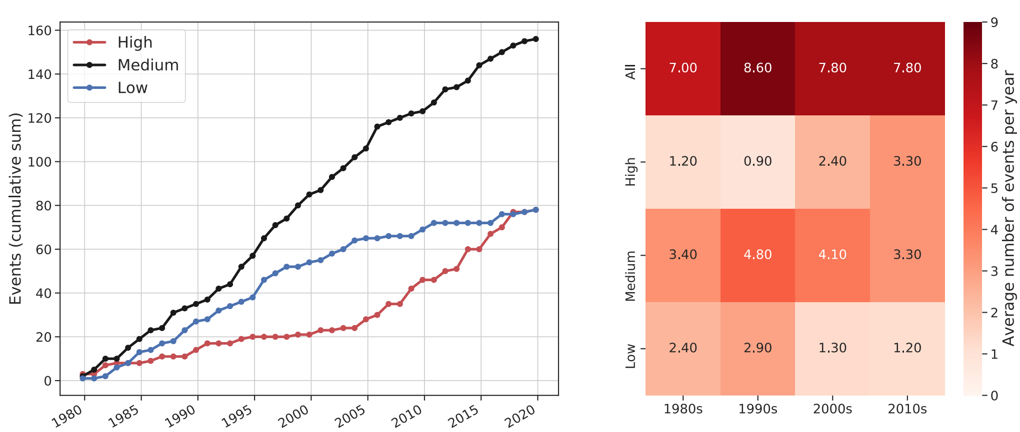


FIG. 11. (Left) Cumulative sum of high (red), medium (black), and low (blue) efficiency events for each winter season, and (right) decadal changes in the average number of events per year.



Accepted for publication in *Journal of Climate*. DOI 10.1175/JCLI-D-21-0852.1.

## 4. Conclusions and discussion

In this paper, we applied an Arctic energy budget perspective to understanding how winter-season synoptic-scale tropospheric weather events influence surface heating. We defined a new metric for surface heating efficiency, $E_{\mathrm{trop}}$, which approximately measures the fraction of the anomalous net tropospheric energy source (NTES) during flux events that reaches the surface (land, ocean, or sea ice) in the Arctic-wide area average. It is important to note that this interpretation of $E_{\mathrm{trop}}$ is most relevant to periods in which tropospheric energy flux ($F_{\mathrm{trop}}$) anomalies are large. We computed the mean $E_{\mathrm{trop}}$ over $F_{\mathrm{trop}}$ events, periods where $F_{\mathrm{trop}}$ is likely the dominant driver of anomalous surface fluxes, over the period January 1980 to March 2020. The $F_{\mathrm{trop}}$ events were then separated into three efficiency-based categories: high, medium, and low-efficiency. A summary schematic of the vertical and temporal structure of each event composite is provided in Fig. 10.

In high-efficiency events, bottom-heavy (i.e., concentrated in the lower troposphere) anomalous poleward $F_{\mathrm{trop}}$—mainly in the Atlantic sector between 20°W and 80°E—occurs in the presence of reduced Atlantic sector sea ice concentration (SIC). Reduced SIC results in reduced lower-tropospheric stability and the implied enhanced turbulent mixing contributes to further near-surface warming (i.e., mixing the warm and moist air aloft to the surface). A majority of the anomalous NTES goes into surface heating, dominated by surface sensible and latent heat fluxes (SHLH) as a result of reduced near-surface vertical gradients in temperature and specific humidity over areas of open ocean and partial sea ice. SIC is further reduced and is slow to recover as positive temperature anomalies persist.

In medium-efficiency events, the Arctic is subject to the same bottom-heavy poleward $F_{\mathrm{trop}}$ profile as in high-efficiency events, but this occurs in the presence of anomalously high Atlantic sector SIC and lower-tropospheric stability; as a result, reduced turbulent mixing limits near-surface warming. Approximately half of the anomalous NTES goes into surface heating, with comparable contributions from DLR and SHLH anomalies. Lower-tropospheric stability reduces and negative SIC anomalies emerge; however, near climatological temperatures allow SIC to quickly recover relative to high-efficiency events.

In low-efficiency events, the anomalous poleward $F_{\mathrm{trop}}$ is more uniform both zonally and vertically (above 925 hPa), and occurs in the presence of increased Atlantic sector SIC and an anomalously cold troposphere with increased lower-tropospheric stability. The combination of poleward $F_{\mathrm{trop}}$





Accepted for publication in *Journal of Climate*. DOI 10.1175/JCLI-D-21-0852.1.

anomalies extending deep into the upper troposphere and reduced turbulent mixing results in an approximate uniform warming of the troposphere. A minority of the anomalous NTES goes into surface heating, mainly through increased DLR. Tropospheric temperatures cool to below climatology, and sea ice quickly recovers to above climatology after a brief reduction.

This work suggests an alternative chain of causality by which the atmosphere drives Arctic winter surface warming. Much of the recent literature on synoptic-scale tropospheric heating events (e.g., D.-S. R. Park et al. 2015; H.-S. Park et al. 2015; Woods and Caballero 2016; Gong et al. 2017; Lee et al. 2017) argues that increased DLR, associated with the anomalously warm and moist atmosphere, primarily drives the surface response [i.e., the net surface flux (NSF)] and found little preconditioning of the Arctic surface. Our results instead show that the impact of individual $F_{\mathrm{trop}}$ events on surface heating varies tremendously depending on two main factors: (1) the preconditioning of the Arctic surface, and (2) the vertical structure of $F_{\mathrm{trop}}$. Together these determine the efficiency of surface heating primarily through the suppression of polar cap–averaged climatological upward turbulent heat fluxes. The anomalous SHLH is four times larger in the high-efficiency composite than the low-efficiency composite (see Fig. 9), due to the combination of bottom-heavy atmospheric heating and preconditioned weak stratification. Note that while individual high-efficiency events are associated with greater surface *heating*, the surface *warming* (i.e., temperature change) is similar in all three events (see Fig. 3). Instead, the greater surface heating in high-efficiency events results in reduced ocean cooling or slower sea ice growth. It is only in the longer term (seasonal or greater) that the accumulated effect of more high-efficiency events would manifest as anomalously warm temperatures.

Regional differences can help reconcile our results with recent literature (e.g., D.-S. R. Park et al. 2015; H.-S. Park et al. 2015; Woods and Caballero 2016; Gong et al. 2017; Lee et al. 2017). While DLR anomalies are found to dominate in areas of sea ice and land, consistent with the aforementioned literature, the anomalous polar cap–averaged DLR is in fact smaller than anomalous polar cap–averaged SHLH for all but the low-efficiency composite and is nearly the same across all event types. Additionally, differences in SHLH anomalies between events are equally large in areas of open ocean and partial sea ice. We suggest that DLR is primarily a diagnostic of lower-tropospheric air temperature and is not a very useful indicator of the causality of surface warming. Additionally, we found a weak preconditioning signal in composites of all events (not





Accepted for publication in *Journal of Climate*. DOI 10.1175/JCLI-D-21-0852.1.

shown), possibly explaining why the initial state of the Arctic surface appears unimportant in the aforementioned literature. Our results are consistent with Chen et al. (2018), who found a larger and more persistent surface response during events preceded by low SIC anomalies.

A potential limitation of our results is the substantial uncertainty in SHLH over areas of sea ice in reanalysis data (e.g., Taylor et al. 2018; Graham et al. 2019a). Our results showing that SHLH anomalies explain the majority of $E_{\text{trop}}$ differences between events should be relatively insensitive to these biases so long as the biases are independently distributed across all event types. Evaluating this would be an interesting avenue for future work.

Our results also show that clouds are not a primary factor in determining surface heating efficiency. Interestingly, increased cloud fractions are largest in low-efficiency events, and both surface and TOA cloud radiative effects (CRE) are relatively small and decrease with increasing $E_{\text{trop}}$. Clouds are thus a small mitigating factor in the efficiency compared to the large range in SHLH. Negative low cloud anomalies in high and medium-efficiency events are inconsistent with recent work using satellite data that find increased cloud amounts in moist intrusion events (Johansson et al. 2017) and over areas of decreased stability (e.g., Yu et al. 2019). However, errors in the relatively small CRE anomalies would likely not impact our results.

The trends we found in the relative frequency of high vs. low-efficiency events may have played a role in the recent winter trends in Arctic surface temperature and sea ice. Despite a lack of trends in the total number of $F_{\text{trop}}$ events, from the period 1980–1999 to 2000–2019, high-efficiency events have increased by approximately two events per year while low-efficiency have decreased by approximately two events per year. This result indicates that the atmosphere is becoming increasingly efficient at heating the Arctic surface during these winter-season events. We speculate that there is both a shift from low to medium-efficiency events (i.e., an increase in bottom-heavy $F_{\text{trop}}$ flux events) and a shift from medium to high-efficiency events (i.e., a decrease in lower-tropospheric stability). An increase in bottom-heavy $F_{\text{trop}}$ events would be consistent with an increase in moist intrusion events (e.g., Woods and Caballero 2016), which have a similar vertical and zonal structure to high and medium-efficiency events. A decrease in lower-tropospheric stability—a signature of Arctic warming (e.g., Cohen et al. 2014)—combined with an increase in bottom-heavy $F_{\text{trop}}$ events could explain why high-efficiency events have increased in frequency, despite little change in medium-efficiency event frequency.





Accepted for publication in *Journal of Climate*. DOI 10.1175/JCLI-D-21-0852.1.

We found this shift towards high-efficiency events despite calculating $E_{\mathrm{trop}}$ from detrended $F_{\mathrm{trop}}$ and NSF anomaly data. We removed long-term trends in order to allay concerns about possible spurious trends in the reanalysis data due to changes in the observing system (e.g., Taylor et al. 2018). While we cannot rule out the possibility that the event-count trends in Fig. 11 are likewise spurious, the fact that they appear in our derived $E_{\mathrm{trop}}$ metric after filtering based on event occurrence is strong evidence that they represent a real physical relationship that is captured in the MERRA-2 data. It is worth noting that the long-term winter-season trend in the MERRA-2 NSF data that we removed is actually downward (atmosphere to ocean) at a rate of 2.15 $\mathrm{W\,m^{-2}\,decade^{-1}}$ (largely driven by a downward trend in SHLH). If this trend were retained in our event calculations, it would have thus produced an even larger trend toward higher efficiency. In ongoing work, we are verifying whether similar trends toward more frequent high-efficiency events are found in historical model simulations, and whether this represents a response to anthropogenic forcing.

Our results suggest an underappreciated atmospheric driver for Arctic amplification of climate change. High-efficiency tropospheric heating events occur preferentially when the Arctic is anomalously warm and unstratified. These events in turn provide more energy to the surface and less upward loss, prolonging the warm and unstratified conditions. This represents a positive feedback loop by which Arctic winter surface warming can be amplified, consistent with our finding of a multi-decadal increase in high-efficiency events. Importantly, this amplification could in principle occur with no change in the large-scale circulation or increase in $F_{\mathrm{trop}}$, nor in cloud feedbacks. Rather, it would manifest in a traditional attribution study as a positive lapse-rate feedback (Pithan and Mauritsen 2014)—the mechanisms for which remain under active debate in the Arctic (e.g., Henry et al. 2021). By taking an event-by-event synoptic view, our efficiency metric provides a new perspective on these processes.

These findings need to be verified in other datasets, and the mechanisms determining efficiency (and their sensitivity to climate change) need to be studied in greater detail. Given that $E_{\mathrm{trop}}$ requires at least daily frequency source data, these calculations are not trivial to undertake. However, we think our results are sufficiently novel and compelling to justify the effort. We are making code available to simplify the adoption of this metric by other groups.

Real insight into the causal relationships between efficiency and Arctic amplification will have to come from climate models, including carefully constructed mechanism-denial experiments. We





Accepted for publication in *Journal of Climate*. DOI 10.1175/JCLI-D-21-0852.1.

are currently validating the simulated $E_{\mathrm{trop}}$ in historical model ensembles to assess the roles of natural variability and anthropogenic forcing. A major goal of future work will be to quantify the effect of efficiency changes on Arctic amplification of future anthropogenic climate change.





Accepted for publication in *Journal of Climate*. DOI 10.1175/JCLI-D-21-0852.1.

*Acknowledgments.* We thank Rodrigo Caballero and two anonymous reviewers for their thoughtful and constructive comments, which strengthened and clarified our paper. MERRA-2 data have been provided by the Global Modeling and Assimilation Office (GMAO) at NASA Goddard Space Flight Center. This work was supported by NSF Awards AGS-1455071 and ICER-2026863.

*Data availability statement.* MERRA-2 data are available through the Goddard Earth Sciences (GES) Data and Information Services Center (DISC) archive (GMAO 2015). The code to reproduce the results is available at https://github.com/cjcardinale/Cardinale-Rose-Efficiency.

## References

Baggett, C., and S. Lee, 2015: Arctic Warming Induced by Tropically Forced Tapping of Available Potential Energy and the Role of the Planetary-Scale Waves. *J. Atmos. Sci.*, **72 (4)**, 1562–1568, https://doi.org/10.1175/JAS-D-14-0334.1.

Baggett, C., and S. Lee, 2017: An Identification of the Mechanisms that Lead to Arctic Warming During Planetary-Scale and Synoptic-Scale Wave Life Cycles. *J. Atmos. Sci.*, **74 (6)**, 1859–1877, https://doi.org/10.1175/JAS-D-16-0156.1.

Barton, N. P., S. A. Klein, J. S. Boyle, and Y. Y. Zhang, 2012: Arctic synoptic regimes: Comparing domain-wide arctic cloud observations with cam4 and cam5 during similar dynamics. *Journal of Geophysical Research: Atmospheres*, **117 (D15)**, https://doi.org/https://doi.org/10.1029/2012JD017589.

Blackport, R., J. A. Screen, K. van der Wiel, and R. Bintanja, 2019: Minimal influence of reduced arctic sea ice on coincident cold winters in mid-latitudes. *Nature Climate Change*, **9 (9)**, 697–704, https://doi.org/10.1038/s41558-019-0551-4.

Boer, G. J., 1982: Diagnostic equations in isobaric coordinates. *Monthly Weather Review*, **110 (12)**, 1801 – 1820, https://doi.org/10.1175/1520-0493(1982)110<1801:DEIIC>2.0.CO;2.

Bosilovich, M. G., S. Akella, L. Coy, and Coauthors, 2015: MERRA-2: Initial evaluation of the climate. Tech. Rep. Series on Global Modeling and Data Assimilation, NASA. Available online at https://gmao.gsfc.nasa.gov/pubs/docs/Bosilovich803.pdf.



Accepted for publication in *Journal of Climate*. DOI 10.1175/JCLI-D-21-0852.1.

Burt, M. A., D. A. Randall, and M. D. Branson, 2016: Dark warming. *Journal of Climate*, **29 (2)**, 705 – 719, https://doi.org/10.1175/JCLI-D-15-0147.1.

Cardinale, C. J., B. E. J. Rose, A. L. Lang, and A. Donohoe, 2021: Stratospheric and tropospheric flux contributions to the polar cap energy budgets. *Journal of Climate*, **34 (11)**, 4261 – 4278, https://doi.org/10.1175/JCLI-D-20-0722.1.

Chen, X., D. Luo, S. B. Feldstein, , and S. Lee, 2018: Impact of winter ural blocking on arctic sea ice: Short-time variability. *J. Climate*, **31 (6)**, 2267–2282, https://doi.org/10.1175/JCLI-D-17-0194.1.

Cohen, J., and Coauthors, 2014: Recent arctic amplification and extreme mid-latitude weather. *Nature Geoscience*, **7**, 627–637, https://doi.org/10.1038/ngeo2234.

Deser, C., R. Tomas, M. Alexander, and D. Lawrence, 2010: The seasonal atmospheric response to projected arctic sea ice loss in the late twenty-first century. *Journal of Climate*, **23 (2)**, 333 – 351, https://doi.org/10.1175/2009JCLI3053.1.

GMAO, 2015: MERRA-2 inst3_3d_asm_Np: 3d,3-Hourly,Instantaneous,Pressure-Level,Assimilation,Assimilated Meteorological Fields V5.12.4. Goddard Earth Sciences Data and Information Services Center (GES DISC), Greenbelt, MD, USA, accessed July 2017, https://doi.org/10.5067/QBZ6MG944HW0.

Doyle, J. G., G. Lesins, C. P. Thackray, C. Perro, G. J. Nott, T. J. Duck, R. Damoah, and J. R. Drummond, 2011: Water vapor intrusions into the high arctic during winter. *Geophysical Research Letters*, **38 (12)**, https://doi.org/https://doi.org/10.1029/2011GL047493.

Eirund, G., A. Possner, and U. Lohmann, 2020: The impact of warm and moist airmass perturbations on arctic mixed-phase stratocumulus. *J. Climate*, **33**, 1–48, https://doi.org/10.1175/JCLI-D-20-0163.1.

Gong, T., S. Feldstein, and S. Lee, 2017: The role of downward infrared radiation in the recent arctic winter warming trend. *Journal of Climate*, **30**, https://doi.org/10.1175/JCLI-D-16-0180.1.

Gong, T., and D. Luo, 2017: Ural blocking as an amplifier of the arctic sea ice decline in winter. *Journal of Climate*, **30 (7)**, 2639 – 2654, https://doi.org/10.1175/JCLI-D-16-0548.1.





Accepted for publication in *Journal of Climate*. DOI 10.1175/JCLI-D-21-0852.1.

Graham, R. M., and Coauthors, 2019a: Evaluation of six atmospheric reanalyses over arctic sea ice from winter to early summer. *Journal of Climate*, **32 (14)**, 4121 – 4143, https://doi.org/10.1175/JCLI-D-18-0643.1.

Graham, R. M., and Coauthors, 2019b: Winter storms accelerate the demise of sea ice in the Atlantic sector of the Arctic Ocean. *Sci Rep*, **9 (1)**, 9222, https://doi.org/10.1038/s41598-019-45574-5.

Graversen, R. G., and M. Burtu, 2016: Arctic amplification enhanced by latent energy transport of atmospheric planetary waves. *Q.J.R. Meteorol. Soc*, **142 (698)**, 2046–2054, https://doi.org/10.1002/qj.2802.

Gulev, S. K., T. Jung, and E. Ruprecht, 2002: Climatology and interannual variability in the intensity of synoptic-scale processes in the north atlantic from the ncep–ncar reanalysis data. *Journal of Climate*, **15 (8)**, 809 – 828, https://doi.org/10.1175/1520-0442(2002)015<0809:CAIVIT>2.0.CO;2.

Hegyi, B. M., and P. C. Taylor, 2018: The unprecedented 2016–2017 arctic sea ice growth season: The crucial role of atmospheric rivers and longwave fluxes. *Geophysical Research Letters*, **45 (10)**, 5204–5212, https://doi.org/https://doi.org/10.1029/2017GL076717.

Henry, M., T. M. Merlis, N. J. Lutsko, and B. E. J. Rose, 2021: Decomposing the drivers of polar amplification with a single-column model. *Journal of Climate*, **34 (6)**, 2355 – 2365, https://doi.org/10.1175/JCLI-D-20-0178.1.

Johansson, E., A. Devasthale, M. Tjernström, A. M. L. Ekman, and T. L'Ecuyer, 2017: Response of the lower troposphere to moisture intrusions into the arctic. *Geophysical Research Letters*, **44 (5)**, 2527–2536, https://doi.org/https://doi.org/10.1002/2017GL072687.

Kayser, M., and Coauthors, 2017: Vertical thermodynamic structure of the troposphere during the norwegian young sea ice expedition (n-ice2015). *Journal of Geophysical Research: Atmospheres*, **122 (20)**, 10,855–10,872, https://doi.org/https://doi.org/10.1002/2016JD026089.

King, J., G. Spreen, S. Gerland, C. Haas, S. Hendricks, L. Kaleschke, and C. Wang, 2017: Sea-ice thickness from field measurements in the northwestern barents sea. *Journal of Geophysical Research: Oceans*, **122 (2)**, 1497–1512, https://doi.org/https://doi.org/10.1002/2016JC012199.



Accepted for publication in *Journal of Climate*. DOI 10.1175/JCLI-D-21-0852.1.

Komatsu, K. K., V. A. Alexeev, I. A. Repina, and Y. Tachibana, 2018: Poleward upgliding siberian atmospheric rivers over sea ice heat up arctic upper air. *Scientific Reports*, **8 (1)**, 2872, https://doi.org/10.1038/s41598-018-21159-6.

Lee, S., T. Gong, S. B. Feldstein, J. A. Screen, and I. Simmonds, 2017: Revisiting the cause of the 1989–2009 arctic surface warming using the surface energy budget: Downward infrared radiation dominates the surface fluxes. *Geophysical Research Letters*, **44 (20)**, 10,654–10,661, https://doi.org/https://doi.org/10.1002/2017GL075375.

Liu, Y., and J. R. Key, 2016: Assessment of arctic cloud cover anomalies in atmospheric reanalysis products using satellite data. *Journal of Climate*, **29 (17)**, 6065 – 6083, https://doi.org/10.1175/JCLI-D-15-0861.1.

Liu, Y., J. R. Key, S. Vavrus, and C. Woods, 2018: Time evolution of the cloud response to moisture intrusions into the arctic during winter. *Journal of Climate*, **31 (22)**, 9389 – 9405, https://doi.org/10.1175/JCLI-D-17-0896.1.

Luo, B., D. Luo, L. Wu, L. Zhong, and I. Simmonds, 2017: Atmospheric circulation patterns which promote winter arctic sea ice decline. *Environmental Research Letters*, **12 (5)**, 054 017, https://doi.org/10.1088/1748-9326/aa69d0.

Luo, B., L. Wu, D. Luo, A. Dai, and I. Simmonds, 2019: The winter midlatitude-arctic interaction: effects of north atlantic sst and high-latitude blocking on arctic sea ice and eurasian cooling. *Climate Dynamics*, **52 (5)**, 2981–3004, https://doi.org/10.1007/s00382-018-4301-5.

Luo, D., Y. Xiao, Y. Yao, A. Dai, I. Simmonds, and C. L. E. Franzke, 2016: Impact of ural blocking on winter warm arctic–cold eurasian anomalies. part i: Blocking-induced amplification. *Journal of Climate*, **29 (11)**, 3925 – 3947, https://doi.org/10.1175/JCLI-D-15-0611.1.

McCarty, W., L. Coy, R. Gelaro, A. Huang, D. Merkova, E. B. Smith, M. Seinkiewicz, and K. Wargan, 2016: MERRA-2 input observations: Summary and assessment. Tech. Rep. Series on Global Modeling and Data Assimilation, NASA. Available online at https://gmao.gsfc.nasa.gov/pubs/docs/McCarty885.pdf.



Accepted for publication in *Journal of Climate*. DOI 10.1175/JCLI-D-21-0852.1.

Overland, J. E., and Coauthors, 2021: How do intermittency and simultaneous processes obfuscate the arctic influence on midlatitude winter extreme weather events? *Environmental Research Letters*, **16 (4)**, 043 002, https://doi.org/10.1088/1748-9326/abdb5d.

D.-S. R. Park, S. Lee, and S. B. Feldstein, 2015: Attribution of the Recent Winter Sea Ice Decline over the Atlantic Sector of the Arctic Ocean. *J. Climate*, **28 (10)**, 4027–4033, https://doi.org/10.1175/JCLI-D-15-0042.1.

H.-S. Park, S. Lee, S.-W. Son, S. B. Feldstein, and Y. Kosaka, 2015: The Impact of Poleward Moisture and Sensible Heat Flux on Arctic Winter Sea Ice Variability. *J. Climate*, **28 (13)**, 5030–5040, https://doi.org/10.1175/JCLI-D-15-0074.1.

Peings, Y., 2019: Ural blocking as a driver of early-winter stratospheric warmings. *Geophysical Research Letters*, **46 (10)**, 5460–5468, https://doi.org/https://doi.org/10.1029/2019GL082097.

Pithan, F., and T. Mauritsen, 2014: Arctic amplification dominated by temperature feedbacks in contemporary climate models. *Nature Geoscience*, **7 (3)**, 181–184, https://doi.org/10.1038/ngeo2071.

Rinke, A., M. Maturilli, R. M. Graham, H. Matthes, D. Handorf, L. Cohen, S. R. Hudson, and J. C. Moore, 2017: Extreme cyclone events in the arctic: Wintertime variability and trends. *Environmental Research Letters*, **12 (9)**, 094 006, https://doi.org/10.1088/1748-9326/aa7def.

Screen, J. A., and I. Simmonds, 2010a: The central role of diminishing sea ice in recent arctic temperature amplification. *Nature*, **464 (7293)**, 1334–1337, https://doi.org/https://doi.org/10.1038/nature09051.

Screen, J. A., and I. Simmonds, 2010b: Increasing fall-winter energy loss from the arctic ocean and its role in arctic temperature amplification. *Geophysical Research Letters*, **37 (16)**, https://doi.org/https://doi.org/10.1029/2010GL044136.

Sokolowsky, G. A., and Coauthors, 2020: Contributions to the surface downwelling longwave irradiance during arctic winter at utqiaġvik (barrow), alaska. *Journal of Climate*, **33 (11)**, 4555–4577, https://doi.org/10.1175/JCLI-D-18-0876.1.

Solomon, A., M. D. Shupe, O. Persson, H. Morrison, T. Yamaguchi, P. M. Caldwell, and G. de Boer, 2014: The sensitivity of springtime arctic mixed-phase stratocumulus clouds to surface-layer





Accepted for publication in *Journal of Climate*. DOI 10.1175/JCLI-D-21-0852.1.

and cloud-top inversion-layer moisture sources. *Journal of the Atmospheric Sciences*, **71 (2)**, 574 – 595, https://doi.org/10.1175/JAS-D-13-0179.1.

Solomon, A., M. D. Shupe, P. O. G. Persson, and H. Morrison, 2011: Moisture and dynamical interactions maintaining decoupled arctic mixed-phase stratocumulus in the presence of a humidity inversion. *Atmospheric Chemistry and Physics*, **11 (19)**, 10 127–10 148, https://doi.org/10.5194/acp-11-10127-2011.

Stroeve, J., M. Serreze, M. Holland, J. Kay, J. Malanik, and A. Barrett, 2012: The arctic's rapidly shrinking sea ice cover: A research synthesis. *Climatic Change*, **110**, 1005–1027, https://doi.org/10.1007/s10584-011-0101-1.

Stroeve, J. C., D. Schroder, M. Tsamados, and D. Feltham, 2018: Warm winter, thin ice? *The Cryosphere*, **12 (5)**, 1791–1809, https://doi.org/10.5194/tc-12-1791-2018.

Taylor, P. C., B. M. Hegyi, R. C. Boeke, and L. N. Boisvert, 2018: On the increasing importance of air-sea exchanges in a thawing arctic: A review. *Atmosphere*, **9 (2)**, https://doi.org/10.3390/atmos9020041.

Taylor, P. C., S. Kato, K.-M. Xu, and M. Cai, 2015: Covariance between arctic sea ice and clouds within atmospheric state regimes at the satellite footprint level. *Journal of Geophysical Research: Atmospheres*, **120 (24)**, 12 656–12 678, https://doi.org/https://doi.org/10.1002/2015JD023520.

Tyrlis, E., E. Manzini, J. Bader, J. Ukita, H. Nakamura, and D. Matei, 2019: Ural blocking driving extreme arctic sea ice loss, cold eurasia, and stratospheric vortex weakening in autumn and early winter 2016–2017. *Journal of Geophysical Research: Atmospheres*, **124 (21)**, 11 313–11 329, https://doi.org/https://doi.org/10.1029/2019JD031085.

Valkonen, E., J. Cassano, and E. Cassano, 2021: Arctic cyclones and their interactions with the declining sea ice: A recent climatology. *Journal of Geophysical Research: Atmospheres*, **126 (12)**, e2020JD034 366, https://doi.org/https://doi.org/10.1029/2020JD034366.

Vargas Zeppetello, L. R., A. Donohoe, and D. S. Battisti, 2019: Does surface temperature respond to or determine downwelling longwave radiation? *Geophysical Research Letters*, **46 (5)**, 2781–2789, https://doi.org/https://doi.org/10.1029/2019GL082220.





Accepted for publication in *Journal of Climate*. DOI 10.1175/JCLI-D-21-0852.1.

Vihma, T., 2014: Effects of arctic sea ice decline on weather and climate: A review. *Surveys in Geophysics*, **35 (5)**, 1175–1214, https://doi.org/10.1007/s10712-014-9284-0.

Woods, C., and R. Caballero, 2016: The Role of Moist Intrusions in Winter Arctic Warming and Sea Ice Decline. *J. Climate*, **29 (12)**, 4473–4485, https://doi.org/10.1175/JCLI-D-15-0773.1.

Woods, C., R. Caballero, and G. Svensson, 2013: Large-scale circulation associated with moisture intrusions into the arctic during winter. *Geophysical Research Letters*, **40 (17)**, 4717–4721, https://doi.org/https://doi.org/10.1002/grl.50912.

Yoo, C., S. Lee, and S. Feldstein, 2012: Mechanisms of arctic surface air temperature change in response to the madden-julian oscillation. *J. Climate*, **25**, 5777–5790, https://doi.org/10.1175/JCLI-D-11-00566.1.

You, C., M. Tjernström, and A. Devasthale, 2021: Warm-air advection over melting sea-ice: A lagrangian case study. *Boundary-Layer Meteorology*, **179 (1)**, 99–116, https://doi.org/10.1007/s10546-020-00590-1.

Yu, Y., P. C. Taylor, and M. Cai, 2019: Seasonal variations of arctic low-level clouds and its linkage to sea ice seasonal variations. *Journal of Geophysical Research: Atmospheres*, **124 (22)**, 12 206–12 226, https://doi.org/https://doi.org/10.1029/2019JD031014.

Zhong, L., L. Hua, and D. Luo, 2018: Local and external moisture sources for the arctic warming over the barents–kara seas. *Journal of Climate*, **31 (5)**, 1963 – 1982, https://doi.org/10.1175/JCLI-D-17-0203.1.





Accepted for publication in *Journal of Climate*. DOI 10.1175/JCLI-D-21-0852.1.